

## *Insight-HXMT* View of the BHC Swift J1727.8-1613 during its outburst in 2023

KAUSHIK CHATTERJEE,<sup>1</sup> SANTANU MONDAL,<sup>2</sup> CHANDRA B. SINGH,<sup>1</sup> AND MUTSUMI SUGIZAKI<sup>3</sup>

<sup>1</sup>South-Western Institute For Astronomy Research, Yunnan University, University Town, Chenggong, Kunming 650500, China

<sup>2</sup>Indian Institute of Astrophysics, 2nd Block Koramangala, Bengaluru 560034, Karnataka, India

<sup>3</sup>National Astronomical Observatories, Chinese Academy of Sciences, 20A Datun Road, Chaoyang District, Beijing 100012, China

Submitted to AAS

### ABSTRACT

The transient Galactic black hole candidate Swift J1727.8-1613 went through an outburst for the very first time that started in August 2023 and lasted for almost 6 months. We study the timing and spectral properties of this source using publicly available archival *Insight-HXMT* data for the first 10 observation IDs that last from MJD 60181 to 60198 with a total of 92 exposures for all three energy bands. We extracted the quasi-periodic oscillation properties by model fitting the power density spectrum and from those properties we designate that the QPOs are type-C in nature. We also conclude that the origin of the QPOs could be the shock instabilities in the transonic advective accretion flows around black holes. The spectral analysis was performed using simultaneous data from the three on-board instruments LE, ME, and HE of *Insight-HXMT* in the broad energy band of 2 – 150 keV. To achieve the best fit, spectral fitting required a combination of models e.g. interstellar absorption, power-law, multi-color disk-blackbody continuum, gaussian emission/absorption, and reflection by neutral material. From the spectral properties, we found that the source was in an intermediate state at the start of the analysis period and was making a transition toward the softer states. The inner edge of the accretion disk moved inward in progressive days following the spectral nature. We found that the source has a high inclination. The average hydrogen column density estimated from the model fitting is  $0.27^{+0.08}_{-0.17} \times 10^{22} \text{ cm}^{-2}$ .

**Keywords:** X-rays: binaries – stars: black holes – stars: individual (Swift J1727.8-1613) – accretion, accretion disk – shock – radiation

### 1. INTRODUCTION

Stellar-mass black holes (SBHs) are one of the end products of the death of massive stars. They reside in binary systems where a companion star supplies matter and during accretion they emit radiation. A significant amount of their radiation comes out in the form of X-rays, therefore, they are called black hole X-ray binaries (BHXRBS). Depending on the mass of the companion star, they can be mainly of two types: low-mass X-ray binaries (LMXRBS) or high-mass X-ray binaries (HMXRBs). The LMXRBs consist of type-A

or later type of stars, whereas the HMXRBs consist of giant O or B-type of stars (White et al. 1995; Tetarenko et al. 2016). During the transfer of mass from the companion, matter accumulates at a distance from the BH due to insufficient viscosity to drive the matter inward, which is called the pile-up radius (Chakrabarti et al. 2019; Chatterjee et al. 2022). Due to the accumulation of more matter, the temperature will rise. The gradual increase in temperature develops instability at the pile-up radius, which further increases the viscosity. At some point in time when the accumulated matter gains enough viscosity to push forward, accretion starts. On the other hand, irradiation of the accumulated matter at the outer boundary by the central object can also trigger mass accretion when the temperature of the accumulated matter crosses a critical limit (King & Ritter 1998; Mondal 2020). Thus, these systems make ideal laboratories for studying the physics of accretion. The BHXRBS mostly stay in a quiet dormant state when their flux remains at a very low detection level. Episodically, the radiation level increases by a very large factor and they become easily detectable, which is known as an outburst

Corresponding author: Kaushik Chatterjee

kaushik@ynu.edu.cn, mails.kc.physics@gmail.com

santanu.mondal@iiap.res.in

chandrasingh@ynu.edu.cn

mutsumi@nao.cas.cn

(Remillard & McClintock 2006). The X-ray luminosity increases by several orders of magnitude during an outburst when compared to a quiescence. Depending on the nature of the outburst, the sources are classified into two types: persistent and transient sources. Most of the BHXRBs are transient type of sources. They stay in the dormant state for most of their lifetimes. The luminosity becomes  $\sim 10^{35}$  erg s<sup>-1</sup> during episodic outbursting phase.

During the onset of an outburst, the flux in the light curve changes noticeably. Based on its nature, the outbursts are divided into two types (Debnath et al. 2010): fast rise slow decay (FRSD) and slow rise slow decay (SRSD). However, there are also some other classified outburst types, e.g., according to Zhang et al. (2019), outbursts can also be classified into glitch, reflare, multippeak, and mini-outburst. There are generally four designated spectral states during a complete BH outburst (Remillard & McClintock 2006). They are known as the hard state (HS), hard intermediate state (HIMS), soft intermediate state (SIMS), and soft state (SS). Generally, when an outburst starts, it starts in the HS. Then it slowly moves toward the SS through the HIMS and SIMS (Belloni et al. 2005, 2011, and references within). After it reaches its SS, the rising phase generally comes to an end and the outburst starts its decaying phase. In the decaying phase, it goes in the opposite direction and reaches the declining HS. When a BH outburst goes through all these states, it is known as a type-I outburst. When the soft state is absent, it is known as a ‘failed’ or type-II outburst.

The radiation spectrum of a BHXRB generally consists of two main components. One is the soft thermal multi-colour blackbody component, which is due to the blackbody radiation of the seed photons in the standard accretion disk (Shakura & Sunyaev 1973; Novikov & Thorne 1973). The other is the hard power-law component, which can extend up to very high energies. The origin of this component is due to the inverse Comptonization of a fraction of seed photons from the disk, which is intercepted by a hot Compton cloud (Sunyaev & Titarchuk 1980, 1985; Haardt & Maraschi 1993; Zdziarski et al. 1993; Titarchuk 1994; Chakrabarti & Titarchuk 1995; Życki et al. 1999). When the outburst is in HS, there is a very small contribution from the thermal blackbody component and mostly the (non)thermal powerlaw component dominates. In SS, the thermal blackbody component becomes dominant while in the intermediate states (HIMS and SIMS), the contribution from the two components stays comparable. Other than these two components, in the case of a high soft state (HSS), there could be the presence of bulk motion Comptonization (BMC) which takes place due to the relativistic speed of matter when it reaches a closer to the BH (Blandford & Payne 1981a,b; Payne & Blandford 1981; Chakrabarti & Titarchuk 1995; Psaltis & Lamb 1997; Borozdin et al. 1999; Psaltis 2001). It was recently observed by Chatterjee et al. (2023) that BMC was present in the radiation spectrum of the black hole candidate (BHC) MAXI J0637-430.

In addition, reprocessing of the Comptonized photons from the Compton cloud by the accretion disk is known as re-

processed radiation (George & Fabian 1991; Ross & Fabian 2005; Garcia & Kallman 2010), which generates reflection spectra. As a result, the Fe  $K\alpha$  emission line at  $\sim 6.4$  keV and a reflection hump above 20 keV may originate. Therefore, the presence of complex features in the spectrum in BHXRBs makes them important to study to understand their origin. This can be achieved by fitting broadband data using multicomponent models. In this regard, high-resolution broadband data of *Insight-HXMT* (Zhang et al. 2020) can be very useful.

Besides rich spectral features and variabilities, temporal properties are equally important to understanding the dynamics of the accreting gas around the BHs. During an outburst, it has been observed that the light curves show very small timescale variabilities, especially in the high-energy bands. The Fourier transformation of the light curve imprints such variabilities as both broadband noise and narrow features in the power density spectrum or PDS (van der Klis 1989). The broadband noise is spread over a large frequency range modeled by power-law function. The narrow feature is a power peak in narrow frequency ranges, known as the quasi-periodic oscillation (QPO), modeled by one or multiple Lorentzian profiles. In BHXRBs, the low-frequency QPOs (LFQPOs) are often observed mainly due to their geometrical origin. Depending on their properties like the frequency ( $\nu$ ),  $Q$ -value ( $= \nu/\delta\nu$ , where  $\delta\nu$  is the full width at half maximum or FWHM), (%RMS, etc., LFQPOs are classified into three different types: type A, B, and C (Casella et al. 2005). Although their origin is still a topic of debate, several ideas were put forward e.g., Lense-Thirring precession (Stella et al. 1999; Ingram et al. 2009), magneto-acoustic waves (Titarchuk et al. 1998), accretion-ejection instability (Tagger & Pellat 1999), shock oscillation model (Molteni et al. 1996; Chakrabarti et al. 2005, 2008, 2015). The shock oscillation model can explain both the spectral and temporal properties simultaneously, which makes it a more comprehensive model.

As both the properties are coming from the same system, and changes in spectral states can also dictate the types of QPOs, it is believed that both are interlinked. A good correlation is observed between the two using just the light curve properties, e.g., the hardness ratio or HR, hardness intensity diagram, or HID (Homan et al. 2001). Some model-fitted approaches also showed that the changes in both properties are due to the interplay between different mass accretion rates or variation in viscosity, can be understood through accretion rate ratio intensity diagram or ARRID (Mondal et al. 2014; Jana et al. 2016; Chatterjee et al. 2020). The RMS-intensity diagram or RID (Munoz-Darias et al. 2011), and hardness ratio-intensity diagram or HRD (Belloni et al. 2005) can also make a link between spectral and temporal properties from pure observational ground.

The BHC Swift J1727.8-1613 was discovered very recently on 24 August 2023 or MJD 60180 (Kennea & Swift Team 2023). MAXI (Matsuoka et al. 2009) detected the source to be very bright with a flux of 7 Crab in the 2 – 20 keV energy range. Since then multi-wavelength follow-up

observations were carried out by several ground-based and space-borne telescope facilities (Baglio et al. 2023; Miller-Jones et al. 2023; Negoro et al. 2023b; O’Connor et al. 2023; Wang & Bellm 2023; Williams-Baldwin et al. 2023). The source is reported to be located at a distance of  $2.7 \pm 0.3$  kpc (MataSanchez et al. 2024) and a mass of  $10 \pm 2 M_{\odot}$  (Svoboda et al. 2024). The revelation of the presence of hydrogen and helium emission lines in the optical spectrum led to its classification as an LMXRB (Castro-Tirado et al. 2023). The X-ray spectrum and other properties point to its nature as a BHXRB (Liu et al. 2023; Sunyaev et al. 2023). This was supported strongly after the detection of type C QPOs (Palmer & Parsotan 2023; Draghis et al. 2023; Bollemeijer et al. 2023; Mereminskiy et al. 2023) and a flat radio spectrum (Miller-Jones et al. 2023; Bright et al. 2023). There is X-ray monitoring of the source by *NICER*, *NuSTAR*, *Insight-HXMT*, *IXPE*, etc. Using *IXPE* data on September 7, 2023, Veledina et al. (2023) estimated its polarization with a polarization degree (PD) of  $4.1\% \pm 0.2\%$  and polarization angle (PA) of  $2^{\circ}.2 \pm 1^{\circ}.3$ . There was a further polarization study of the source by Ingram et al. (2023).

At the starting of the outburst, the spectral nature was consistent with a hard state with a power-law photon index ( $\Gamma$ )  $\sim 1.5 - 1.7$  (Liu et al. 2023). Later, using the *NICER* observations, Bollemeijer et al. (2023) reported the softening of the spectrum with a substantial contribution of the soft blackbody component after 25 days from the starting of the outburst. The presence of LFQPOs was reported by Draghis et al. (2023) and the evolution of LFQPOs at the high energy band using *AstroSat* data was reported by Nandi et al. (2024). The source also showed soft time lag of  $0.014 \pm 0.001$  sec between energy bands of 3 – 10 and 0.5 – 3 keV on August 29 2023 (MJD 60185) (Debnath et al. (2023) using *NICER* data). With reflection spectroscopy, authors found the disk inclination to be  $\sim 87^{\circ}$ . However, to date, there is no detailed study on the origin of the spectral and temporal properties of the source, which prompted us to analyze the broadband X-ray data from *Insight-HXMT*.

The paper is organized as follows: in §2, we describe the observation, data selection, reduction, and analysis procedures. In §3, we portray the spectral and temporal properties and observed results. In §4, we discuss the possible physical origin of our result and connection between observed features. Finally, in §5, we summarize the results and draw conclusions.

## 2. OBSERVATION, DATA SELECTION, REDUCTION, AND ANALYSIS

The source is being extensively monitored by various X-ray satellites, as discussed earlier. For this study, we use China’s first dedicated X-ray satellite *Insight-HXMT* (HXMT; Zhang et al. 2014, 2020) data. In the subsequent subsections, we discuss the data selection, reduction, and analysis, respectively.

### 2.1. Data Selection

**Table 1.** List of observations used for this work. Here, column 1 lists the observation IDs. Columns 2 and 3 denote the start and end date of observations, while columns 4 and 5 refer to corresponding MJDs. Column 6 gives the exposure time of each observation.

Obs. Id.	Start Date	End Date	Start MJD	Stop MJD	Exp. (s)
(1)	(2)	(3)	(4)	(5)	(6)
P0614338001	2023-08-25	2023-08-27	60181.3410	60183.0597	148495
P0614338002	2023-08-27	2023-08-28	60183.0597	60184.2327	137343
P0614338003	2023-08-29	2023-08-31	60185.3075	60187.1589	159958
P0614338004	2023-08-31	2023-09-02	60187.1588	60189.0765	165684
P0614338005	2023-09-02	2023-09-04	60189.0765	60191.0601	171384
P0614338006	2023-09-04	2023-09-06	60191.0601	60193.4447	206034
P0614338008	2023-09-07	2023-09-08	60194.0350	60195.0926	91378
P0614338009	2023-09-08	2023-09-09	60195.0926	60196.0840	85659
P0614338010	2023-09-09	2023-09-10	60196.0840	60197.0754	85653
P0614338011	2023-09-10	2023-09-11	60197.0753	60198.0667	85650

The source was regularly monitored by the *Insight-HXMT* satellite. In the [data archive](#), observations are available on-demand. We found that there are a total of 34 observation IDs available<sup>1</sup>. Out of those available 31 observation IDs, we took the first 10 observation IDs. However, unlike other X-ray satellite data, each observation ID in *HXMT* has several exposures. Also, some of the observation IDs have continuous observations of about 2 to 3 days. We found that for these first 10 observation IDs, each of them has a minimum of 7 to a maximum of 18 exposures. Initially, we perform the analysis of all the exposures for the first 3 observation IDs and found no significant change in the parameters of spectral fits in the consecutive exposures. Therefore, we avoid fitting every exposure of each observation ID. The details of the selected data are given in Table 1.

### 2.2. Data Reduction

The main scientific instrument of *Insight-HXMT* is an array of 18 NaI/CSI phoswich scintillation detectors, each of which covers an effective area of 286 cm<sup>2</sup>. The satellite has three instruments or payloads: High Energy (HE; Liu et al. 2020), Medium Energy (ME; Chen et al. 2020), and Low Energy (LE; Cao et al. 2020). They have an effective area of 5100, 952, and 384 cm<sup>2</sup> and cover an energy range of 20 – 250, 5 – 30, and 1 – 15 keV, respectively.

After downloading on-demand level-1 data from the archive, we produced cleaned level-2 data for science analysis. The processing of cleaning raw data was done in the following way. We first installed the *HXMTDAS*<sup>2</sup> v2.05. Using this software, we run the `hpipeline` command using proper input and output directories. This pipeline performs several subsequent automatic commands for all three instruments under some given conditions. Some conditions were set to get a good time interval, e.g., elevation angle  $> 10^{\circ}$ ; geomagnetic cutoff rigidity  $> 8$  GeV; pointing offset angle  $< 0.04^{\circ}$ ;  $> 600$  sec away from the South Atlantic Anomaly

<sup>1</sup> Although 3 of them were not downloadable

<sup>2</sup> <http://hxmt.org/index.php/usersp/dataan>

(SAA). All these commands altogether extract and clean the raw data and produce cleaned and analyzable science products<sup>3</sup>. The specific commands `hespecgen`, `mespecgen`, and `lespecgen` produce the spectra for HE, ME, and LE instruments. Whereas, the `helcgen`, `melcgen`, and `lelcgen` tasks produce the light curve files for the three instruments. `herispgen`, `merispgen`, and `lerispgen` produce corresponding response files. The background subtraction for both the timing and spectral data was performed using the commands `hebkmap`, `mebkmap`, and `lebkmap` for instruments HE, ME, and LE, respectively. For the  $\chi^2$  fit-statistics in XSPEC, we grouped the spectrum using the `grppha` task of FTOOLS to a minimum of 30 counts per bin. We also set the time bin size to 0.01 sec to produce the light curves for generating PDS and QPOs.

Using the cleaned spectra and light curves, we further fitted and analyzed to extract the outburst properties, which are discussed in the next section.

### 2.3. Data Analysis

We have downloaded the daily average light curve of *MAXI/GSC*<sup>5</sup> from the archive to study the outburst profile in addition to *Insight-HXMT*. Using the unbinned light curves from LE, ME, and HE modules, we have first produced 0.01 sec time-binned light curves. Then the power density spectrum (PDS) was generated using the fast Fourier transformation (FFT) technique in the `powspec` task of the XRONOS package in the HEASoft software. Each observation's data was subdivided into several intervals, each of which contains 8192 newbins. First, the PDS for each interval is generated and then they are averaged to make a resultant PDS. The PDS is normalized in a way that their integral can give the RMS-squared fractional variability. The white noise level is subtracted and a geometrical rebinning of -1.02 is used. For some data, we needed to use a geometrical rebinning of -1.05 to have a prominent QPO-like nature in the PDS. We fit the QPO using single or multiple Lorentzian model components in `powspec` to extract QPO properties like frequency ( $\nu_{qpo}$ ), full-width at half maximum or FWHM, and normalization. For several observations, we have found the presence of single or multiple harmonics. We have also extracted their properties using the same fitting method. We have fitted the light curves of all the exposures of the listed 10 observations. We report them in the result section.

For the spectral analysis, we have used the same LE, ME, and HE modules and fitted the broadband data in the 2 – 150 keV energy band. The best is achieved by using the combination of `disk blackbody`, `power-law`, `gaussian`, and `pexrav` models. For some observations, we needed to add a `gabs` model to achieve the best fit. For interstellar absorption, we have used the `tbabs` model. Since we simultaneously fit all three modules, we have included a `constant` to normalize the three

resultant fittings. The following two model combinations are used: i) `constant*tbabs*gabs*(diskbb + power-law + gaussian + pexrav)`, ii) `constant*tbabs*(diskbb + power-law + gaussian + pexrav)` (for which `gabs` was not required). The spectral analysis was done for the exposures are marked with ‘\*’ in Table 2. We did not do the spectral analysis for all epochs as spectral variability was not present within such a small timescale (intraday) like the variability in the light curves. We report them in the result section.

We note that light curves for the LE instrument were not produced for some exposures. Therefore, we represented only those exposures' MJDs in Table 3 for which all three light curves were available for analysis for uniformity.

## 3. RESULTS

Using the timing and spectral analysis, we have studied the accretion flow properties of the very recent 2023 outburst of the BHC Swift J1727.8-1613. We studied the QPO properties of the source during the outburst as well as the spectral nature and radiation properties using *Insight-HXMT* data. We broadly discuss the results in the next two sections.

### 3.1. Temporal Properties

Here, we discuss the evolution of the flux and hardness ratio, and QPO properties during the first 10 observation IDs of the outburst.

#### 3.1.1 Outburst Profile and Hardness Ratio

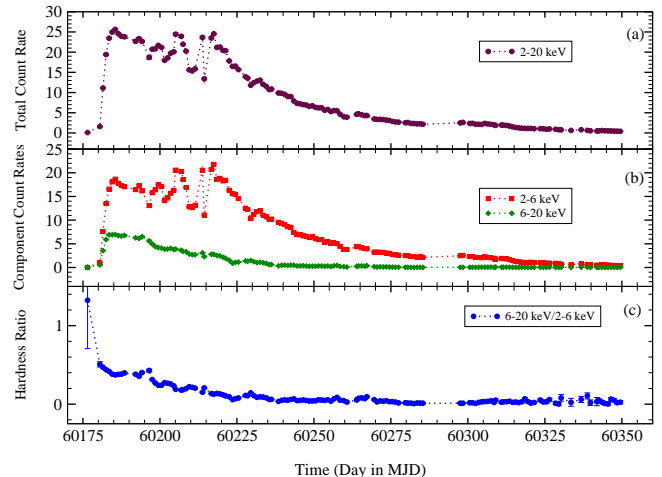


**Figure 1.** Variation of the (a) MAXI/GSC 2 – 20 keV count rate, (b) MAXI/GSC 2 – 6 and 6 – 20 keV count rates, and (c) hardness ratio with time. The HR is the ratio of the 6 – 20 keV count rate to the 2 – 6 keV count rate of the MAXI/GSC data.

Figure 1 shows the variation of the flux obtained from *MAXI/GSC* during the outburst. The outburst started roughly at around MJD 60180 (2023 August 24), when its flux came out of quiescence. The *MAXI/GSC* flux started to rise after this date, as we can notice from panel (a) of Figure 1. Within

<sup>3</sup> This is discussed in the *HXMT manual*<sup>4</sup> in full details

<sup>5</sup> [http://maxi.riken.jp/star\\_data/J1727-162/J1727-162.html](http://maxi.riken.jp/star_data/J1727-162/J1727-162.html)

five days, the flux increased very rapidly and the total flux reached its peak on MJD 60185 (2023 August 29). After that, the flux started to decrease very slowly, except for the period from MJD 60200 to 60225, where the flux showed a significant change. In panel (b), we show the variations of the count rates with time in the 2 – 6 and 6 – 20 keV energy bands. We notice that, after MJD 60185, the hard flux (i.e., 6 – 20 keV) decreased very slowly, whereas, the soft 2 – 6 keV flux showed a lot of variation just like the total 2 – 20 keV flux. On MJD 60185 the 2 – 20 keV and hard 6 – 20 keV fluxes reached their peak values, whereas, the soft flux reached its peak much later at around MJD 60217. This suggests that the variation in the total count rate is mainly due to the variation of the soft component. After this period, the soft flux also decreased slowly till the end of the outburst and entered again into the quiescence phase.

In panel (c), we show the variation of the hardness ratio, which is the ratio of the hard ( $F_H$ ) 6 – 20 keV to the soft ( $F_S$ ) 2 – 6 keV flux. At the start of the outburst, the HR was  $\sim 0.5$  and then it gradually decreased to MJD 60235 as the outburst progressed. After that, the HR became almost constant, although decreasing very slowly to  $\sim 0.025$  at the end of the considered data of the outburst on MJD 60350. The way HR is defined, when this value is on the higher side, the spectral nature of the source is hard. This is the general case when an outburst is starting. When this value is low, there is dominance of soft flux over hard flux and the spectral nature would be soft. Without studying the detailed spectral analysis, HR provides a quick idea about the spectral nature of an outburst. However, for this source, we notice that HR was a little higher at the onset of the outburst, where the hard flux was also comparable to the soft flux. However, after a few days, soft flux completely took over the hard flux, and the HR was also not high. Depending on the HR value, we propose that the source was already in the SIMS after the onset of the outburst. After MJD 60185, it made a transition into the SS. Since we are not analyzing the full duration of the outburst, it is not the scope of the paper to study the full spectral classification. We only define the spectral state of the source based on the duration of which data is used in this work.

### 3.1.2. Quasi Periodic Oscillations (QPOs)

As described in §2, we used the 0.01 sec time-binned light curves from all three bands (LE, ME, and HE) and produced the PDS to study QPOs. We find that QPO nature was present in all the light curves in all three energy bands. In Figure 2, we show the variation of the QPO frequency ( $\nu_{qpo}$ ) for the 10 different obs. IDs as stated before. We first checked the first obs. ID P0614338001. It has several exposure IDs (given in Table 2). While we fit every exposure of this obs ID, we found that the QPO frequency was changing even within this small period. This is the reason we fitted all the light curves of the exposures of the obs IDs that we have taken for analysis. We find that for every single obs ID, the  $\nu_{qpo}$  showed significant variation. Figure 2(a), (b), (c) show the

### Evolution of QPO frequency in different observation IDs

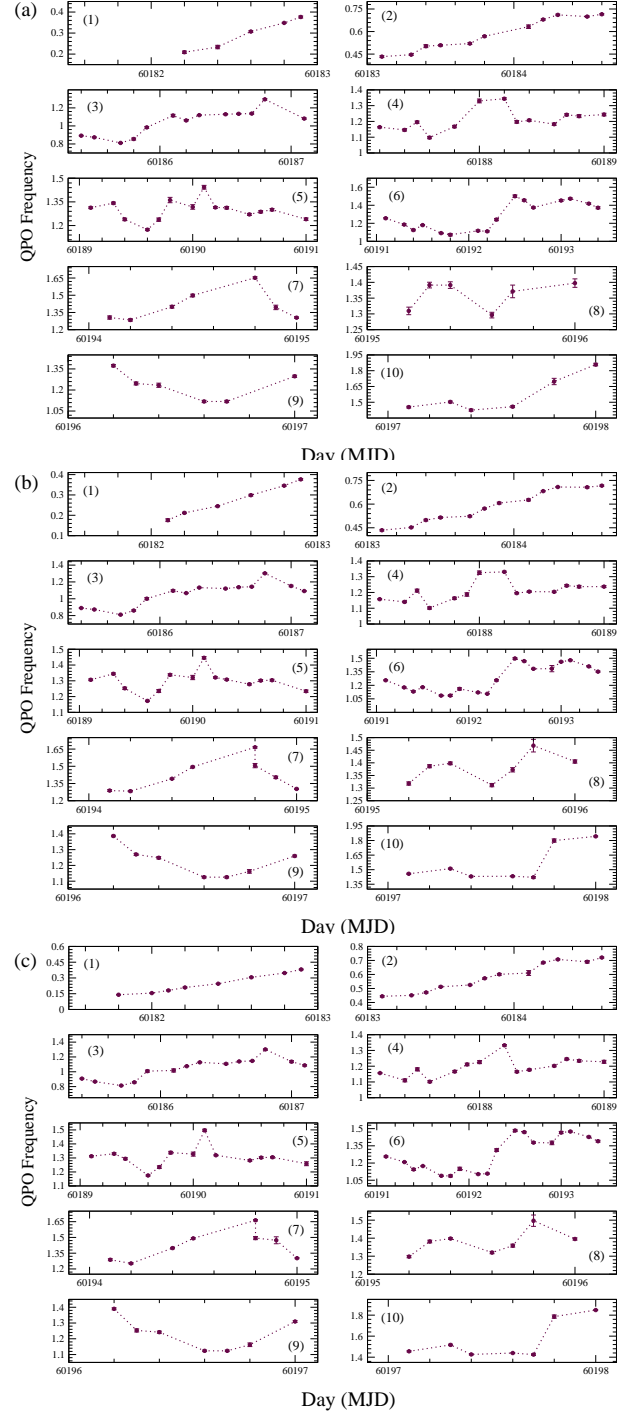


**Figure 2.** Evolution of QPO frequencies (Hz) with time. Here we have shown three different plots for (a) LE, (b) ME, and (c) HE instruments. Panels 1–10 in each of the three of these plots (a, b, c) represent the  $\nu_{qpo}$  variation for the 10 observation IDs we used.

variations of the  $\nu_{qpo}$  with time for 10 different obs IDs for LE, ME, and HE respectively.

## Evolution of RMS (%) with QPO frequency and time

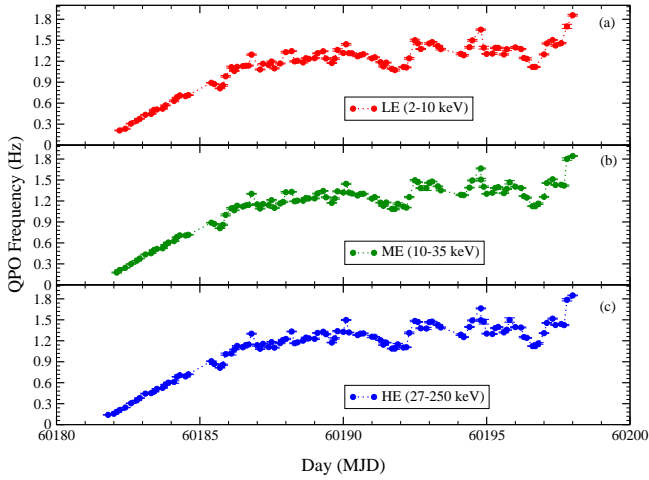


**Figure 3.** Evolution of QPO frequency with time during the whole period of analysis for (a) LE, (b) ME, and (c) HE.

In Figure 3, we show the evolution of the  $\nu_{qpo}$  for the total duration of our analysis period. In (a), (b), and (c) panels the variations are for LE, ME, and HE respectively. We find that the QPO frequencies were  $\sim 0.23 \pm 0.008$ ,  $0.24 \pm 0.002$ , and  $0.24 \pm 0.002$  Hz for LE, ME, and HE on the starting day of our analysis. After this day, the  $\nu_{qpo}$  shows a rapid increase with time till  $\sim$  MJD 60187 when  $\nu_{qpo}$  was  $\sim 1.2$ Hz for all the three bands. After this date, it increased very slowly till MJD  $\sim 60190$  when  $\nu_{qpo}$  was  $\sim 1.45$ . Then it decreased for a very short period until it rapidly increased to 1.5Hz again in all three bands. After that, it showed varying nature till MJD  $\sim 60197$ , and then it finally increased again. We have discussed the possible reason behind this nature in the next section.

Using the PDS fitting, we extracted some information (e.g., full-width at half maximum (FWHM), Normalization (LN)) of QPOs. We also extracted source and background count rates for the exposures. Using these estimates, we calculated the  $Q$ -value and RMS that represent the sharpness of the QPO and the fractional variability in the PDS, respectively. These values are listed in Table 3 in columns 5–7 ( $Q$ -value) and 8–10 (RMS) for LE, ME, and HE respectively.

In Figure 4, we show a 3-D representation of the evolution of QPO and RMS with time. In the LE band (Fig. 4a), the RMS was higher at the start of the analysis period and it then gradually decreased. In the ME band (Fig. 4b), it increased from the onset of the analysis period for some time and then again decreased. The HE band (Fig. 4c) shows a similar trend as in LE band. Since the QPO nature has already been reported in the recent paper by Yu et al. (2024), we are not focusing on the classification of the QPO nature. However, by the values of both  $Q$ -factor and RMS, it can be said that the QPO is type-C in nature for all the exposures reported here.

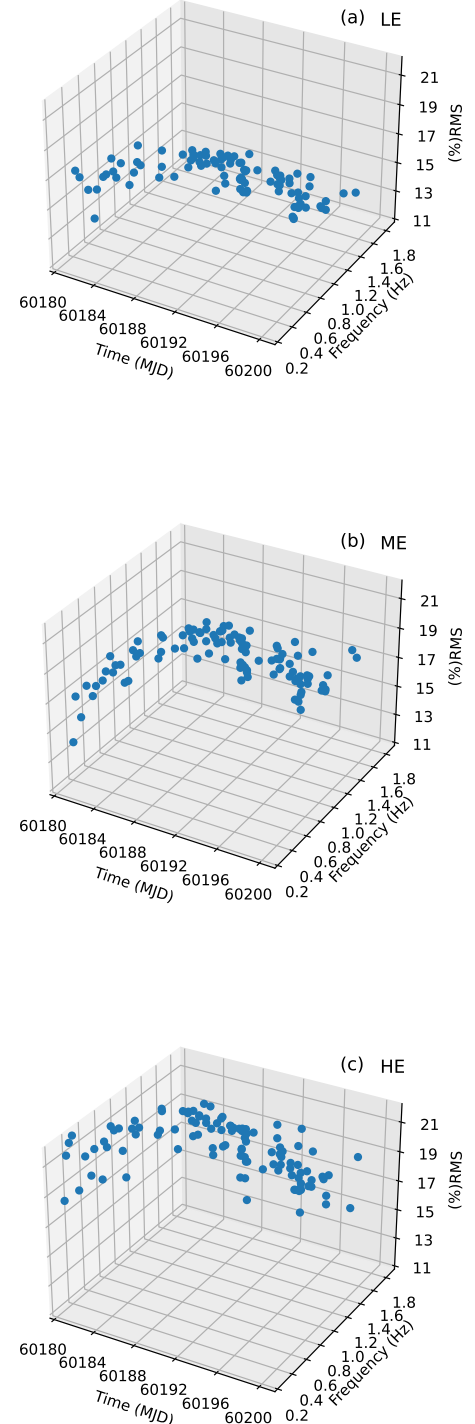


**Figure 4.** 3-D representation of the variation of  $\nu_{qpo}$  and (%RMS) with time (MJD) for (a) LE, (b) ME, and (c) HE.

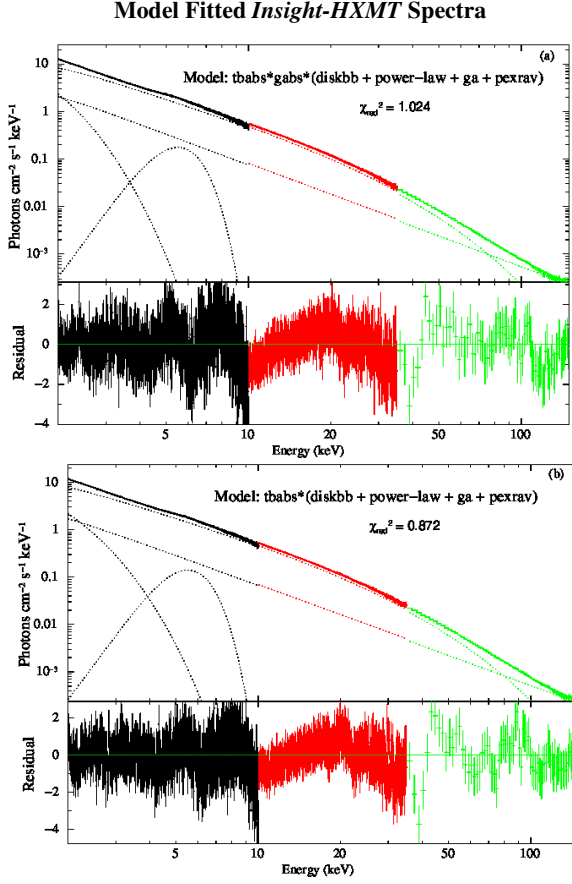


**Figure 5.** Model fitted spectrally analyzed unfolded spectra. (a) is for observation ID. P061433800501 (Exposure: P061433800501-20230902-01-01) for which the *gabs* model was required to achieve the best fit. (b) is for the observation ID. P061433800601 (exposure: P061433800601-20230904-01-01) for which the *gabs* model was not required to achieve the best fit.

### 3.2. Spectral Properties

Along with the timing properties, studying the spectral properties provides more insights on the nature of the outburst. With the available *Insight-HXMT* data, we analyzed the source for a total of 32 exposures. These exposure IDs are marked with a ‘\*’ sign in the 1st column of Table 2. An extensive spectral analysis on this source has not been done so far. We perform a detailed spectral analysis on this source for the first time using HXMT data. We started our spectral analysis from MJD 60181.4. We have simultaneously used LE+ME+HE in the 2 – 150 keV energy band (LE in 2–10, ME in 10–35, and HE in 35–150 keV) for our spectral fitting for all the selected exposure IDs.

We first fitted the data with phenomenological *diskbb* and *power-law* models. We used the multiplicative *tbabs* model to account for the interstellar absorption. Our model read as `constant*tbabs(diskbb + powerlaw)` in XSPEC. The `constant` is taken to normalize between three different instruments in LE, ME, and HE. We found that the fit was not statistically ac-

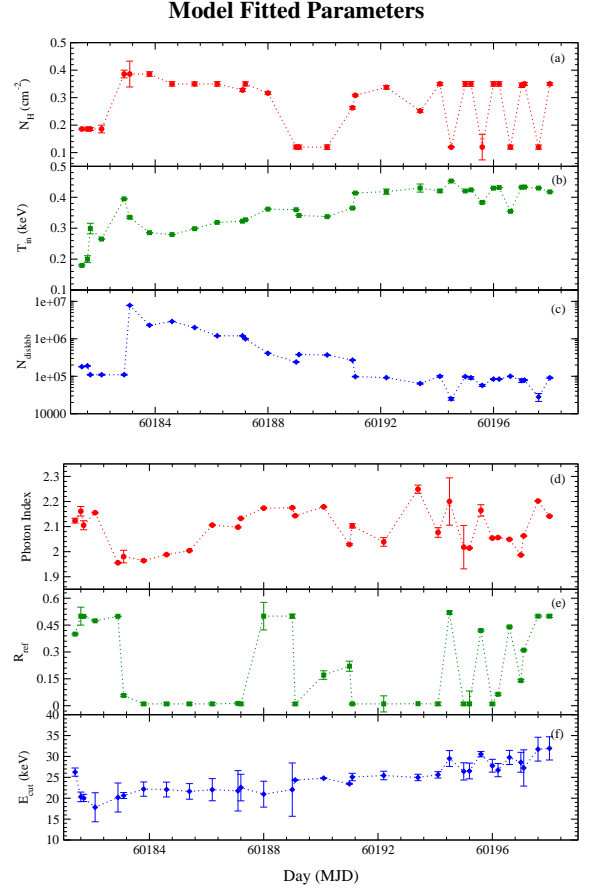


**Figure 6.** Variation of spectrally fitted properties (a) hydrogen column density ( $n_H$ ), (b) inner-disk temperature ( $T_{in}$ ), (c) diskbb normalization, (d) Photon Index ( $\Gamma$ ), (e) reflection fraction ( $R_{ref}$ ), and (f) cutoff energy ( $E_{cut}$ ) with time.

ceptable. There was a clear sign of the Gaussian feature in the unfolded spectrum around 5 – 6 keV. Also, there was a hump-like feature  $\sim 20$  keV. Besides these features, the absorption feature was noticed below 2 keV. Thus, we refitted the data using the model combination as `constant*tbabs*gabs(diskbb + power-law + ga + pexrav)`. Here, the *gabs* model takes care of the low energy absorption feature, while the *ga* and *pexrav* models take care of the contribution from the Gaussian and hump-like nature, as mentioned above. In Fig. 5a, we show the best-fitted unfolded spectrum using this model combination for the observation ID P061433800501 (Exposure ID: P061433800501-20230902-01-01), where  $\chi^2/DOF \sim 1$ . After some exposure, we found that the *gabs* model was not needed anymore to achieve the best fit. Then, the model combination in XSPEC reads as `constant*tbabs(diskbb + power-law + ga + pexrav)`. In Figure 5b, we show an unfolded best-fitted spectrum using the later model combination. This is for the observation ID. P061433800601 (exposure ID: P061433800601-20230904-01-01), for which  $\chi^2/DOF \sim 0.9$ .

For our overall spectral analysis with the two sets of models, we have assumed  $abund = 1.0$  and  $Fe_{abund} = 1.0$  in the `pexrav` model with redshift ( $z$ ) = 0. From the spectral fitting, we extracted various properties of the source during the first few days of the outburst. We estimated the inner-disk temperature ( $T_{in}$ ), photon index of power-law ( $\Gamma$ ) which is the slope of the spectrum. We found that from MJD 60181.4 to 60190.0, there was an absorption feature at  $\sim 1.65 - 1.95$  keV. After this day, the `gabs` model was no longer needed to achieve the best fit. The  $T_{in}$  was  $\sim 0.180 \pm 0.002$  keV at the start of the outburst and it gradually increased to  $\sim 0.420 \pm 0.003$  keV on the last day of our analysis. The  $\Gamma$  of the power-law model was  $2.12 \pm 0.01$  on the first day. From the variation of the light curve in Figure 1, we notice that the flux was already very high at the starting date of our analysis (HXMT data was available from this date too). The value of  $T_{in}$  and  $\Gamma$  indicate that the source has already transitioned past its HS and could be in an intermediate state. As the outburst progressed,  $T_{in}$  became higher with the norm of the `diskbb` model decreased as the outburst progressed.  $\Gamma$  of the power-law model varied in the range 2.10 – 2.16 for the first few days then decreased a little and then again slowly increased to 2.20. We found the presence of a broad Gaussian line, with the line energy varying between 5.2 – 5.75 keV. We did not link the  $\Gamma$  of the `pexrav` model to the  $\Gamma$  of the power-law model, as we noticed that the spectral slope was different between low and high energies. The  $\Gamma$  of the `pexrav` model varied in the range of 0.94 – 1.9. The  $E_{cut}$  varied in the range of  $\sim 20 - 32$  keV. The  $\cos(i)$  parameter varied in the range 0.05 – 0.1 for most of the exposures except for the first two, where it was  $\sim 0.5$ , and 0.2, respectively. This could be due to the degeneracy of the parameter space. The column density of H ( $N_H$ ) varied in the range  $0.1 - 0.35 \times 10^{22} \text{ cm}^{-2}$  during the entire duration of this analysis. In Figure 6(a-f), we show the variations of the spectral model fitted parameters with time.

### 3.3. Correlation between spectral and timing properties

The QPO frequency can be produced from the oscillation of the Compton corona, which can also be the origin of the hard power-law photons that extend the spectrum to higher energies. Therefore, these two features might be interlinked or correlated. It has been previously seen that the QPO frequency ( $\nu_{qpo}$ ) and  $\Gamma$  show a positive correlation for some of the sources during their active outbursting phase (Vignarca et al. 2003; Shaposhnikov & Titarchuk 2009; Stiele et al. 2013). We also tried to find out if there are any correlations between these two properties. In Figure 7, we show the variations of the photon index with the QPO frequency for the three energy bands. Considering these points, we have found a positive correlation between  $\Gamma$  and  $\nu_{qpo}$ . Using both the Pearson-Linear and Spearman-Rank correlation methods, we found correlation coefficients for the three energy bands as shown in the table below.

Photon Index ( $\Gamma$ ) vs QPO frequency ( $\nu_{qpo}$ )

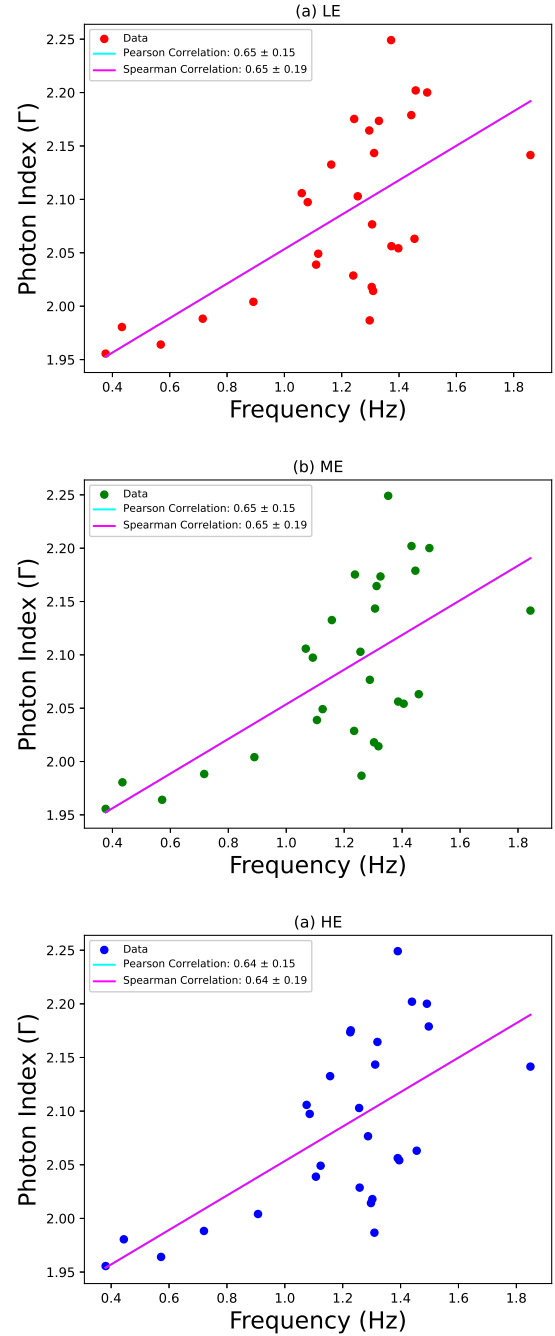


**Figure 7.** Variation of photon index of power-law ( $\Gamma$ ) with QPO frequency ( $\nu_{qpo}$ ) for (a) LE, (b) ME, and (c) HE instruments. Here,  $\Gamma$  is the spectral fitted index using combined LE+ME+HE data.

	Pearson-Linear	Spearman-Rank
LE	$0.65 \pm 0.15$	$0.65 \pm 0.19$
ME	$0.65 \pm 0.15$	$0.65 \pm 0.19$
HE	$0.64 \pm 0.15$	$0.64 \pm 0.19$

#### 4. DISCUSSIONS

The Galactic black hole Swift J1727.8-1613 went through an outburst recently in 2023. We have used *Insight-HXMT* data for our both spectral and timing studies from MJD 60181.4 to 60198.0. The evolution of the light curve makes the outburst nature of the source a fast-rise slow decay type. After the onset of the outburst, the flux reached its peak value very fast within 5 days. Using the 0.01 sec time-binned light curves from the three instruments of HXMT (LE, ME, and HE), we studied the source's timing properties. Using the spectra files from these three instruments, we also studied the spectral properties of this source by analyzing combined LE+ME+HE spectra in the 2 – 150 keV broad energy range.

##### 4.1. Propagation of Shock

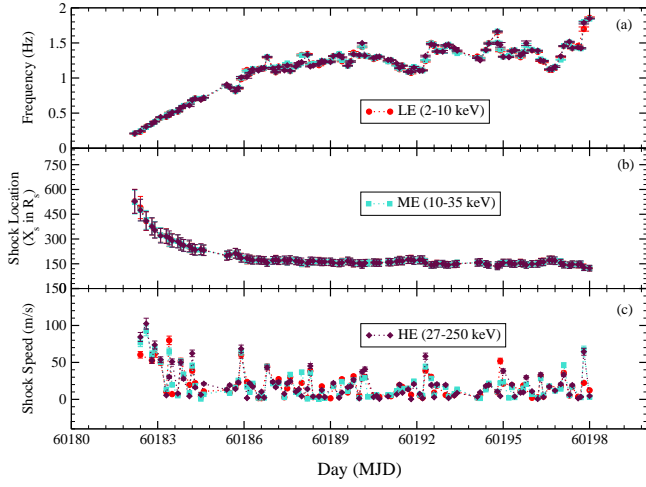


**Figure 8.** Variation of shock properties with time in accordance with  $\nu_{qpo}$ . In (a) the variation of  $\nu_{qpo}$  with time and in (b) and (c) we show the variations of the shock location ( $X_s$ ), and shock speed ( $v$ ) with time.

Quasi-periodic oscillation is one of the most important and common phenomena for stellar mass black holes. For this newly discovered source, we analyzed a total of 342 light curves (114 for LE, ME, and HE each). However, in some of the exposures, light curves were not produced properly. There were a total of 92 exposures which commonly produced LE, ME, and HE light curves. We list those data in Table 3. Finally, we analyzed 276 lightcurves. We found the presence of QPO in all of these light curves, and they showed rapid evolution in frequency in this short analysis period. The QPO frequency ( $\nu_{qpo}$ ) showed an increase in frequency within even a single day. The evolution of the QPO frequency has been discussed broadly in the result section. It showed an increasing trend from the start of our analysis. From the variation of QPO frequency, ( $\%$ )RMS, and  $Q$ -factor, the nature of the QPO is designated to be type-C. Although the QPOs are extensively studied in the literature, their origin requires in depth modeling.

Here, we would like to focus on the physical scenario that explains the origin of QPOs due to the shock instabilities in advective flows around BHs. Accretion onto BH is transonic flow with possibility of multiple sonic points (Chakrabarti 1989). The matter from the companion need not necessarily be only Keplerian. There could be a supply of matter which has angular momentum distribution deviated from the Keplerian one. This is the sub-Keplerian component. Such a lower angular momentum component of infalling matter gets accreted in a free-fall timescale. Due to the tug of war between the gravitational force and centrifugal force, this matter could virtually stop at some distance from the BH and undergo shock transition, creating a post-shock region. Depending on the flow properties, the standing shocks forms (Chakrabarti 1989; Singh et al. 2022 and references therein). This approach can well describe the observed spectral and temporal properties of BHs (Debnath et al. 2014; Mondal et al. 2014, Chatterjee et al. 2020, 2021, 2023). According to Molteni et al. (1996), the shock can be oscillatory due to the presence of cooling. This was later shown in simulation by Garain et al. (2014). During the oscillation when the cooling timescale due to the Comptonization process and the heating timescale matches, QPOs originate (see Chakrabarti et al. 2015). Additionally, it has also been observed by the authors that once the QPO sets in, it gets locked for a week or more depending on the above condition. From the expressions of infall and cooling timescales, we get that the QPO frequency ( $\nu_{qpo}$ ) can be estimated using the relation (Molteni et al. 1996; Chakrabarti & Manickam 2000; Chakrabarti et al. 2004),

$$\nu_{qpo} = \frac{c^3}{2GM_{BH}} \frac{1}{RX_s(X_s - 1)^{1/2}} \text{ Hz.} \quad (1)$$

Where  $c$ ,  $G$ ,  $M_{BH}$ ,  $X_s$ , and  $R$  are the speed of light, gravitational constant, the mass of the BH, location of the shock, and the ratio of matter densities in post-shock to pre-shock regions ( $\rho_+/\rho_-$ ) respectively. From our timing analysis, we already extracted the information about QPO frequency ( $\nu_{qpo}$ ). Using the above relation, we estimated the shock location during the outburst. According to Chakrabarti et al. (2005),  $X_s$  can be located anywhere above  $10 r_s$  depending on the flow parameters producing shocks. The shock forms far away  $\sim 1000 r_s$  when the spectral nature of the ongoing outburst is hard and decreases gradually in the progressive days as cooling increases (Mondal et al. 2015). Using Eq. 1, we found that the shock was far away from the BH at the start of the outburst (see Figure 8b). It then significantly decreased as the QPO frequency increased rapidly during the initial few days. Close to MJD 60185, when the  $\nu_{qpo}$  stopped increasing, and the shock location started to decrease very slowly. The values of the shock location along with QPO frequency are given in Table 3.

If the time of the first exposure ID was taken to be 0, and the shock location as  $X_{s0}$  and after time  $t$ , if the shock is at  $X_s$ , then the velocity of the movement of the shock would be given by the equation (Chakrabarti et al. 2005)

$$v = \frac{X_{s0} - X_s}{t} \text{ ms}^{-1}. \quad (2)$$

Using this relation, we have estimated the velocity of the movement of the shock. The estimated shock velocities are given in Figure 8c, which is a few tens of m/s in accord with the previous estimations (Chakrabarti et al. 2005; Mondal et al. 2015). We find that the shock velocity has varied within this period. At the beginning, it attained higher values when the  $X_s$  was also larger, however decreasing significantly afterwards. It slowed down as the shock moved inwards, along with some fluctuations. This can be due to the limitation of assuming constant velocity of the shock propagation.

#### 4.2. Evolution of the physical configuration and spectral nature

From the spectral properties, we have seen that the  $T_{in}$  was low initially and then gradually increased. The exact opposite trend was observed for the Normalization of the `diskbb` model. The norm of `diskbb` model varies as

$$N_{diskbb} = \left( \frac{R_{in}}{D_{10}} \right)^2 \cos i \quad (3)$$

where,  $R_{in}$ ,  $D_{10}$  are the inner-disk radius of the accretion disk and the distance of the source in 10 kpc unit.  $i$  is the inclination angle of the accretion disk to the observer. Assuming that  $D_{10}$  and  $\theta$  do not change during an outburst, the relation could be shortened like  $R_{in} \sim N_{diskbb}^{1/2}$ . For our case, except for one exposure, the inclination varied in a narrow range of  $78-86^\circ$ . Thus, as the  $N_{diskbb}$  decreased, it means the inner edge of the disk moved closer to the BH, which agrees with the fact that  $T_{in}$  increased as the disk moved closer. Furthermore, this also supports the properties we showed from the timing analysis that the shrinking of post-shock region with time.

Looking at the spectral parameters, and also the location of the shock, we designate that the source was already in an intermediate state at the start of our analysis period. As the outburst progressed, it was transitioning towards softer states. From the values of the parameter  $\cos(i)$  of the `pexrav` model, we find that the inclination of the disk was  $> 60^\circ$ , which makes this source a highly inclined system. The hydrogen column density ( $N_H$ ) showed a variation, which is common for Galactic black hole binaries unless the system is heavily obscured, which has recently been found for the newly discovered BH Swift J151857.0-572147 (Mondal et al. 2024). The average  $N_H$  has an average value of  $0.27_{-0.17}^{+0.08} \times 10^{22} \text{ cm}^{-2}$ .

### 5. SUMMARY AND CONCLUSIONS

We have studied the timing and spectral properties of the BHC Swift J1727.8-1613 during its recent outburst in 2023. We show the evolution of the light curve along with

its hardness ratio for the entire duration of the outburst using archival MAXI/GSC data. Studying the entire evolution of the outburst was not the scope of this paper. Using the *Insight-HXMT* data, we chose the first ten observation IDs for our analysis. We use all the exposures from those observation IDs and selective exposures for timing and spectral analysis, respectively. Using 0.01 s time-binned light curves from all three instruments of HXMT, i.e., LE, ME, and HE, we studied the QPO properties by producing a power density spectrum. The QPO properties were extracted with the use of Lorentzian model. For spectral analysis, we use LE + ME + HE spectrum files in the broad 2 – 150 keV energy band. We found that the models i) `constant*tbabs*gabs*(diskbb + power-law + gaussian + pexrav)` (for those for which `gabs` was required), ii) `constant*tbabs*(diskbb + power-law + gaussian + pexrav)` fits the spectra best. From our analysis, we conclude that:

(i) Quasi-periodic oscillations were present during the entire period of our analysis, which showed evolution in QPO frequency.

(ii) The  $Q$ -factor and  $RMS$  help designate the nature of the QPOs as type-C.

(iii) QPOs originated from the shock instabilities that was formed by matter having an angular momentum distribution deviated from the Keplerian distribution. As the shock moved inwards, the QPO frequency was observed to increase.

(iv) With the shock moving inwards, the spectral nature of the source was transitioning towards the softer states, after it started in the intermediate state at the onset of the analysis period.

(v) The spectral and temporal properties correlate to each other which makes our claim stronger about the origin of QPOs.

(vi) This source has a high inclination.

(vii) The hydrogen column density varied in the range of  $0.10 - 0.35 \times 10^{22} \text{ cm}^{-2}$ , which is quite common for interstellar absorption of Galactic black holes.

### 6. DATA AVAILABILITY

This work has made use of public data from several satellite/instrument archives and has made use of software from the HEASARC, which is developed and monitored by the Astrophysics Science Division at NASA/GSFC and the High Energy Astrophysics Division of the Smithsonian Astrophysical Observatory. This work made use of the data from the *Insight-HXMT* mission, a project funded by the China National Space Administration (CNSA) and the Chinese Academy of Sciences (CAS).

### 7. ACKNOWLEDGEMENTS

KC acknowledges support from the SWIFAR postdoctoral fund of Yunnan University. SM acknowledges the Ramanujan Fellowship (# RJF/2020/000113) by SERB-DST, Govt. of India for this research. CBS is supported by the Na-

tional Natural Science Foundation of China under grant no. 12073021.

## REFERENCES

- Baglio, M. C., Casella, P., Testa, V., et al. 2023, *The Astronomer's Telegram*, 16225, 1
- Belloni, T., Homan, J., Casella, P., van der Klis, M., et al., 2005, *A&A*, 440, 207
- Belloni, T. M., Motta, S. E., & Muñoz-Darias, T., 2011, *Bulletin of the Astronomical Society of India*, 39, 409
- Blandford, R. D., & Payne, D. G., 1981a, *MNRAS*, 194, 1033
- Blandford, R. D., & Payne, D. G., 1981b, *MNRAS*, 194, 1041
- Bollemeijer, N., Uttley, P., Buisson, D., et al. 2023, *The Astronomer's Telegram*, 16247, 1
- Borozdin, K., Revnivtsev, M., Trudolyubov, S., Shrader, C., & Titarchuk, L., 1999, *ApJ*, 517, 367
- Bright, J., Farah, W., Fender, R., et al. 2023, *The Astronomer's Telegram*, 16228, 1
- Cao, X., Jiang, W., Meng, B., et al. 2020, *Science China Physics, Mechanics, and Astronomy*, 63, 249504
- Casella, P., Belloni, T., & Stella, L., 2005, *ApJ*, 629, 403
- Castro-Tirado, A. J., Sanchez-Ramirez, R., Caballero-Garcia, M. D., et al. 2023, *The Astronomer's Telegram*, 16208, 1
- Chakrabarti, S. K., 1989, *MNRAS*, 340, 7
- Chakrabarti, S. K., & Titarchuk, L. G., 1995, *ApJ*, 455, 623
- Chakrabarti, S. K., & Manickam, S. G., 2000, *ApJ*, 531, L41
- Chakrabarti, S. K., Acharya, K., & Molteni, D., 2004, *A&A*, 421, 1
- Chakrabarti, S. K., Nandi, A., Debnath, D., Sarkar, R., & Datta, B. G., 2005, preprint (arXiv:astro-ph/0508024)
- Chakrabarti, S. K., Debnath, D., Nandi, A., & Pal, P. S., 2008, *A&A*, 489, L41
- Chakrabarti, S. K., Mondal, S., & Debnath, D., 2015, *MNRAS*, 452, 3451
- Chakrabarti, S. K., Debnath, D., & Nagarkoti, S., 2019, *AdSpR*, 64, 3749
- Chatterjee, K., Debnath, D., Chatterjee, D., Jana, A., Chakrabarti, S. K., 2020, *MNRAS*, 493, 2452
- Chatterjee, K., Debnath, D., Chatterjee, D., Jana, A., et al., 2021, *Ap&SS*, 366, 63
- Chatterjee, K., Debnath, D., Bhowmick, R., Nath, S. K., & Chatterjee, D., 2022, *MNRAS*, 510, 1128
- Chatterjee, K., Debnath, D., Nath, S. K., Chang, S.-K., 2023, *ApJ*, 965, 55
- Chatterjee, K., Debnath, D., Nath, S. K., & Chang, H. -K., 2023, *ApJ*, 965, 55
- Chen, Y., Cui, W., Li, W., et al. 2020, *Science China Physics, Mechanics, and Astronomy*, 63, 249505
- Debnath, D., Chakrabarti, S.K., & Nandi, A., 2010, *A&A*, 520, A98
- Debnath, D., Chakrabarti, S. K., & Mondal, S., 2014, *MNRAS*, 440, L121
- Debnath, D., Nath, S. K., Chatterjee, D., Chatterjee, K., Sen, K., Chang, H. -K., 2023, *The Astronomer's Telegram*, 16287, 1
- Draghis, P. A., Miller, J. M., Homan, J., et al. 2023, *The Astronomer's Telegram*, 16219, 1
- Garain, S., Ghosh, H., & Chakrabarti, S. K., 2014, *MNRAS*, 437, 1329
- Garcia, J., & Kallman, T. R. 2010, *ApJ*, 718, 695
- George, I. M., & Fabian, A. C. 1991, *MNRAS*, 249, 352
- Haardt, F., & Maraschi, L., 1993, *ApJ*, 413, 507
- Homan, J., Wijnands, R., van der Klis, M., Belloni, T., van Paradijs, J., KleinWolt, M., Fender, R., & Mendez, M., 2001, *ApJS*, 132, 377
- Ingram, A., Done, C., & Fragile, P. C., 2009, *MNRAS*, 397, L101
- Ingram, A., Ewing, M., Marinucci, A., et al. 2023, *MNRAS*, doi: 10.1093/mnras/stad2625
- Jana, A., Debnath, D., Chakrabarti, S. K., Mondal, S., & Molla, A. A., 2016, *ApJ*, 819, 107
- Kennea, J. A. & Swift Team 2023, *GCN*, 34540, 1
- King, A. R., & Ritter, H., 1998, *MNRAS*, 293, L42
- Liu, C., Zhang, Y., Li, X., et al. 2020, *Science China Physics, Mechanics, and Astronomy*, 63, 249503
- Liu, H. Y., Li, D. Y., Pan, H. W., et al. 2023, *The Astronomer's Telegram*, 16210, 1
- Mata Sanchez, D., Munoz-Darias, T., Armas Padilla, M., Casares, J., & Torres, M. A. P., 2024, *A&A*, 682, L1
- Matsuoka, M., Kawasaki, K., Ueno, S., et al. 2009, *PASJ*, 61, 999
- Mereminskiy, I., Lutovinov, A., Molkov, S., et al. 2023, *MNRAS*, submitted, arXiv:2310.06697, doi: 10.48550/arXiv.2310.06697
- Miller-Jones, J. C. A., Sivakoff, G. R., Bahramian, A., & Russell, T. D. 2023, *The Astronomer's Telegram*, 16211, 1
- Molteni, D., Sponholz, H., & Chakrabarti, S. K., 1996, *ApJ*, 457, 805
- Mondal, S., Debnath, D., & Chakrabarti, S. K., 2014, *ApJ*, 786, 4
- Mondal, S., Suribhatla, S. P., Chatterjee, K., & Singh, C. B., 2024, *JHEAP*, (preprint: arXiv:2404.09643)
- Mondal, S., 2020, *Advances in Space Research*, 65, 693
- Mondal, S., Chakrabarti, S. K., & Debnath, D., 2015, *ApJ*, 798, 57
- Munoz-Darias, T., Motta, S., & Belloni, T. M., 2011, *MNRAS*, 410, 679
- Nandi, A., Das, S., Majumder, S., et al., 2024, (preprint:arXiv:2404.17160)
- Negoro, H., Serino, M., Nakajima, M., et al. 2023b, *The Astronomer's Telegram*, 16205, 1

- Novikov, I. D., & Thorne, K. S., 1973, in *Black Holes (Les Astres Occlus)*. pp 343–450
- O’Connor, B., Hare, J., Younes, G., et al. 2023, *The Astronomer’s Telegram*, 16207, 1
- Palmer, D. M., & Parsotan, T. M. 2023, *The Astronomer’s Telegram*, 16215, 1
- Payne, D. G., & Blandford, R. D., 1981, *MNRAS*, 196, 781
- Psaltis, D., & Lamb, F. K., 1997, *ApJ*, 488, 881
- Psaltis, D., 2001, *ApJ*, 555, 786
- Remillard, R. A., & McClintock, J. E., 2006, *ARA&A*, 44, 49
- Ross, R. R., & Fabian, A. C. 2005, *MNRAS*, 358, 211
- Shakura, N. I., & Sunyaev, R. A., 1973, *A&A*, 24, 337
- Shaposhnikov, N., & Titarchuk, L., 2009, *ApJ*, 699, 453
- Singh, C. B., Mondal, S., & Garofalo, D., 2022, *MNRAS*, 510, 807
- Stiele, H., Belloni, T. M., Kalemci, E., & Motta, S., 2013, *MNRAS*, 429, 2655
- Stella, L., & Vietri, M., 1998, *ApJ*, 492, L59
- Stella, L., Vietri, M., & Morsink, S. M., 1999, *ApJ*, 524, L63
- Sunyaev, R. A., & Titarchuk, L. G., 1980, *A&A*, 500, 167
- Sunyaev, R. A., & Titarchuk, L. G., 1985, *A&A*, 143, 374
- Sunyaev, R. A., Mereminskiy, I. A., Molkov, S. V., et al. 2023, *The Astronomer’s Telegram*, 16217, 1
- Svoboda, J., Dovciak, M., Steiner, F., Kaaret, P., et al., 2024 ([arxiv preprint](#))
- Tagger, M., & Pellat, R., 1999, *A&A*, 349, 1003
- Tetarenko, B. E., Sivakoff, G. R., Heinke, C. O., & Gladstone, J. C., 2016, *ApJS*, 222, 15
- Titarchuk, L., 1994, *ApJ*, 434, 570
- Titarchuk, L., Lapidus, I., & Muslimov, A., 1998, *ApJ*, 499, 315
- Titarchuk, L., & Osherovich, V., 2000, *ApJ*, 542, L111
- van der Klis, M., 1989, *Annu. Rev. Astron. Astrophys.*, 27, 517
- Veledina, A., Poutanen, J., & Ingram, A. 2013, *ApJ*, 778, 165, doi: 10.1088/0004-637X/778/2/165
- Wang, Y. D., & Bellm, E. C. 2023, *The Astronomer’s Telegram*, 16209, 1
- White N. E., Nagase F., Parmar A. N., 1995, in *X-ray Binaries*. pp 1–57
- Williams-Baldwin, D., Motta, S., Rhodes, L., et al. 2023, *The Astronomer’s Telegram*, 16231, 1
- Vignarca, F., Migliari, S., Belloni, T., Psaltis, D., & van der Klis, M., 2003, *A&A*, 397, 729
- Yu, W., Bu, Q.-C., Zhang, S.-N., Liu, H.-X., Zhang, L., et al., 2024, *MNRAS (arXiv preprint)*
- Zdziarski, A. A., Zycki, P. T., Svensson, R., & Boldt, E., 1993, *ApJ*, 405, 125
- Zhang, S., Lu, F. J., Zhang, S. N., & Li, T. P. 2014, in *Society of Photo-Optical Instrumentation Engineers (SPIE) Conference Series*, Vol. 9144, *Space Telescopes and Instrumentation 2014: Ultraviolet to Gamma Ray*, ed. T. Takahashi, J.-W. A. den Herder, & M. Bautz, 914421
- Zhang, S. -N., et al., 2020, *Science China Physics, Mechanics, and Astronomy* 63, 249502
- Życki, P. T., Done, C., & Smith, D. A., 1999, *MNRAS*, 309, 561

**Table 2.** Start and Stop Time of all the HXMT Exposures

Exposure ID (1)	UT Start (2)	MJD Start (3)	UT Stop (4)	MJD Stop (5)	Average MJD (6)
P061433800101-20230825-01-01*	2023-08-25	60181.3411	2023-08-25	60181.4980	60181.4
P061433800102-20230825-01-01*	2023-08-25	60181.4980	2023-08-25	60181.6301	60181.6
P061433800103-20230825-01-01*	2023-08-25	60181.6301	2023-08-25	60181.7622	60181.7
P061433800104-20230825-01-01	2023-08-25	60181.7622	2023-08-25	60181.8944	60181.8
P061433800105-20230825-01-01	2023-08-25	60181.8944	2023-08-26	60182.0265	60182.0
P061433800106-20230826-02-01*	2023-08-26	60182.0265	2023-08-26	60182.1586	60182.1
P061433800107-20230826-02-01	2023-08-26	60182.1586	2023-08-26	60182.2842	60182.2
P061433800108-20230826-02-01	2023-08-26	60182.2842	2023-08-26	60182.4229	60182.4
P061433800110-20230826-02-01	2023-08-26	60182.5551	2023-08-26	60182.6872	60182.6
P061433800111-20230826-02-01	2023-08-26	60182.6872	2023-08-26	60182.8193	60182.8
P061433800112-20230826-02-01*	2023-08-26	60182.8193	2023-08-26	60182.9515	60182.9
P061433800113-20230826-02-01	2023-08-26	60182.9515	2023-08-27	60183.0598	60183.0
P061433800201-20230827-01-01*	2023-08-27	60183.0597	2023-08-27	60183.2029	60183.1
P061433800202-20230827-01-01	2023-08-27	60183.2029	2023-08-27	60183.3450	60183.3
P061433800203-20230827-01-01	2023-08-27	60183.3450	2023-08-27	60183.4800	60183.4
P061433800204-20230827-01-01	2023-08-27	60183.4800	2023-08-27	60183.6122	60183.5
P061433800205-20230827-01-01	2023-08-27	60183.6122	2023-08-27	60183.7443	60183.7
P061433800206-20230827-01-01*	2023-08-27	60183.7443	2023-08-27	60183.8764	60183.8
P061433800207-20230827-01-01	2023-08-27	60183.8764	2023-08-28	60184.0086	60183.9
P061433800208-20230828-02-01	2023-08-28	60184.0086	2023-08-28	60184.1407	60184.1
P061433800209-20230828-02-01	2023-08-28	60184.1407	2023-08-28	60184.2662	60184.2
P061433800210-20230828-02-01	2023-08-28	60184.2662	2023-08-28	60184.4050	60184.3
P061433800211-20230828-02-01	2023-08-28	60184.4050	2023-08-28	60184.5371	60184.5
P061433800212-20230828-02-01*	2023-08-28	60184.5371	2023-08-28	60184.6494	60184.6
P061433800301-20230829-01-01*	2023-08-29	60185.3075	2023-08-29	60185.4621	60185.4
P061433800302-20230829-01-01	2023-08-29	60185.4621	2023-08-29	60185.5942	60185.5
P061433800303-20230829-01-01	2023-08-29	60185.5942	2023-08-29	60185.7264	60185.7
P061433800304-20230829-01-01	2023-08-29	60185.7264	2023-08-29	60185.8585	60185.8
P061433800305-20230829-01-01	2023-08-29	60185.8585	2023-08-29	60185.9906	60185.9
P061433800306-20230829-01-01	2023-08-29	60185.9906	2023-08-30	60186.1228	60186.1
P061433800307-20230830-02-01*	2023-08-30	60186.1228	2023-08-30	60186.2481	60186.2
P061433800308-20230830-02-01	2023-08-30	60186.2481	2023-08-30	60186.3866	60186.3
P061433800309-20230830-02-01	2023-08-30	60186.3866	2023-08-30	60186.5192	60186.5
P061433800310-20230830-02-01	2023-08-30	60186.5192	2023-08-30	60186.6513	60186.6
P061433800311-20230830-02-01	2023-08-30	60186.6513	2023-08-30	60186.7835	60186.7
P061433800312-20230830-02-01	2023-08-30	60186.7835	2023-08-30	60186.9156	60186.8
P061433800313-20230830-02-01	2023-08-30	60186.9156	2023-08-31	60187.0478	60187.0
P061433800314-20230831-03-01*	2023-08-31	60187.0478	2023-08-31	60187.1589	60187.1
P061433800401-20230831-01-01*	2023-08-31	60187.1589	2023-08-31	60187.3083	60187.2
P061433800402-20230831-01-01	2023-08-31	60187.3083	2023-08-31	60187.4442	60187.4

Continued on next page

Table 2 – continued from previous page

Exposure ID (1)	UT Start (2)	MJD Start (3)	UT Stop (4)	MJD Stop (5)	Average MJD (6)
P061433800403-20230831-01-01	2023-08-31	60187.4442	2023-08-31	60187.5763	60187.5
P061433800404-20230831-01-01	2023-08-31	60187.5763	2023-08-31	60187.7084	60187.6
P061433800405-20230831-01-01	2023-08-31	60187.7084	2023-08-31	60187.8406	60187.8
P061433800406-20230831-01-01	2023-08-31	60187.8406	2023-08-31	60187.9727	60187.9
P061433800407-20230831-01-01*	2023-08-31	60187.9727	2023-09-01	60188.1049	60188.0
P061433800408-20230901-02-01	2023-09-01	60188.1049	2023-09-01	60188.2298	60188.2
P061433800409-20230901-02-01	2023-09-01	60188.2298	2023-09-01	60188.3682	60188.3
P061433800410-20230901-02-01	2023-09-01	60188.3682	2023-09-01	60188.5013	60188.4
P061433800411-20230901-02-01	2023-09-01	60188.5013	2023-09-01	60188.6334	60188.6
P061433800412-20230901-02-01	2023-09-01	60188.6334	2023-09-01	60188.7656	60188.7
P061433800413-20230901-02-01	2023-09-01	60188.7656	2023-09-01	60188.8977	60188.8
P061433800414-20230901-02-01*	2023-09-01	60188.8977	2023-09-02	60189.0765	60189.0
P061433800501-20230902-01-01*	2023-09-02	60189.0765	2023-09-02	60189.2206	60189.1
P061433800502-20230902-01-01	2023-09-02	60189.2206	2023-09-02	60189.3590	60189.3
P061433800503-20230902-01-01	2023-09-02	60189.3590	2023-09-02	60189.4924	60189.4
P061433800504-20230902-01-01	2023-09-02	60189.4924	2023-09-02	60189.6245	60189.6
P061433800505-20230902-01-01	2023-09-02	60189.6245	2023-09-02	60189.7567	60189.7
P061433800506-20230902-01-01	2023-09-02	60189.7567	2023-09-02	60189.8888	60189.8
P061433800507-20230902-01-01	2023-09-02	60189.8888	2023-09-03	60190.0209	60190.0
P061433800508-20230903-02-01*	2023-09-03	60190.0209	2023-09-03	60190.1531	60190.1
P061433800509-20230903-02-01	2023-09-03	60190.1531	2023-09-03	60190.2806	60190.2
P061433800510-20230903-02-01	2023-09-03	60190.2806	2023-09-03	60190.4174	60190.3
P061433800511-20230903-02-01	2023-09-03	60190.4174	2023-09-03	60190.5495	60190.5
P061433800512-20230903-02-01	2023-09-03	60190.5495	2023-09-03	60190.6817	60190.6
P061433800513-20230903-02-01	2023-09-03	60190.6817	2023-09-03	60190.8138	60190.7
P061433800514-20230903-02-01	2023-09-03	60190.8138	2023-09-03	60190.9460	60190.9
P061433800515-20230903-02-01*	2023-09-03	60190.9460	2023-09-04	60191.0601	60191.0
P061433800601-20230904-01-01*	2023-09-04	60191.0601	2023-09-04	60191.2022	60191.1
P061433800602-20230904-01-01	2023-09-04	60191.2022	2023-09-04	60191.3406	60191.3
P061433800603-20230904-01-01	2023-09-04	60191.3406	2023-09-04	60191.4746	60191.4
P061433800604-20230904-01-01	2023-09-04	60191.4746	2023-09-04	60191.6067	60191.5
P061433800605-20230904-01-01	2023-09-04	60191.6067	2023-09-04	60191.7389	60191.7
P061433800606-20230904-01-01	2023-09-04	60191.7389	2023-09-04	60191.8710	60191.8
P061433800607-20230904-01-01	2023-09-04	60191.8710	2023-09-05	60192.0032	60191.9
P061433800608-20230905-02-01	2023-09-05	60192.0032	2023-09-05	60192.1353	60192.1
P061433800609-20230905-02-01*	2023-09-05	60192.1353	2023-09-05	60192.2621	60192.2
P061433800610-20230905-02-01	2023-09-05	60192.2621	2023-09-05	60192.3996	60192.3
P061433800611-20230905-02-01	2023-09-05	60192.3996	2023-09-05	60192.5318	60192.5
P061433800612-20230905-02-01	2023-09-05	60192.5318	2023-09-05	60192.6639	60192.6
P061433800613-20230905-02-01	2023-09-05	60192.6639	2023-09-05	60192.7961	60192.7
P061433800614-20230905-02-01	2023-09-05	60192.7961	2023-09-05	60192.9283	60192.9
P061433800615-20230905-02-01	2023-09-05	60192.9283	2023-09-06	60193.0604	60193.0
P061433800616-20230906-03-01	2023-09-06	60193.0604	2023-09-06	60193.1926	60193.1

Continued on next page

Table 2 – continued from previous page

Exposure ID (1)	UT Start (2)	MJD Start (3)	UT Stop (4)	MJD Stop (5)	Average MJD (6)
P061433800617-20230906-03-01	2023-09-06	60193.1926	2023-09-06	60193.3222	60193.3
P061433800618-20230906-03-01*	2023-09-06	60193.3222	2023-09-06	60193.4448	60193.4
P061433800801-20230907-01-01*	2023-09-07	60194.0351	2023-09-07	60194.1745	60194.1
P061433800802-20230907-01-01	2023-09-07	60194.1745	2023-09-07	60194.3130	60194.2
P061433800803-20230907-01-01	2023-09-07	60194.3130	2023-09-07	60194.4481	60194.4
P061433800804-20230907-01-01*	2023-09-07	60194.4481	2023-09-07	60194.5802	60194.5
P061433800805-20230907-01-01	2023-09-07	60194.7124	2023-09-07	60194.8446	60194.8
P061433800806-20230907-01-01	2023-09-07	60194.7124	2023-09-07	60194.8446	60194.8
P061433800807-20230907-01-01	2023-09-07	60194.8446	2023-09-07	60194.9767	60194.9
P061433800808-20230907-01-01*	2023-09-07	60194.9767	2023-09-08	60195.0927	60195.0
P061433800901-20230908-01-01*	2023-09-08	60195.0927	2023-09-08	60195.2343	60195.2
P061433800902-20230908-01-01	2023-09-08	60195.2343	2023-09-08	60195.3732	60195.3
P061433800903-20230908-01-01	2023-09-08	60195.3732	2023-09-08	60195.5054	60195.4
P061433800904-20230908-01-01*	2023-09-08	60195.5054	2023-09-08	60195.6375	60195.6
P061433800905-20230908-01-01	2023-09-08	60195.6375	2023-09-08	60195.7697	60195.7
P061433800906-20230908-01-01	2023-09-08	60195.7697	2023-09-08	60195.9019	60195.8
P061433800907-20230908-01-01*	2023-09-08	60195.9019	2023-09-09	60196.0841	60196.0
P061433801001-20230909-01-01*	2023-09-09	60196.0841	2023-09-09	60196.2251	60196.2
P061433801002-20230909-01-01	2023-09-09	60196.2251	2023-09-09	60196.3645	60196.3
P061433801003-20230909-01-01	2023-09-09	60196.3645	2023-09-09	60196.4967	60196.4
P061433801004-20230909-01-01*	2023-09-09	60196.4967	2023-09-09	60196.6288	60196.6
P061433801005-20230909-01-01	2023-09-09	60196.6288	2023-09-09	60196.7610	60196.7
P061433801006-20230909-01-01	2023-09-09	60196.7610	2023-09-09	60196.8932	60196.8
P061433801007-20230909-01-01*	2023-09-09	60196.8932	2023-09-10	60197.0754	60197.0
P061433801101-20230910-01-01*	2023-09-10	60197.0754	2023-09-10	60197.2158	60197.1
P061433801102-20230910-01-01	2023-09-10	60197.2158	2023-09-10	60197.3558	60197.3
P061433801103-20230910-01-01	2023-09-10	60197.3558	2023-09-10	60197.4879	60197.4
P061433801104-20230910-01-01*	2023-09-10	60197.4879	2023-09-10	60197.6201	60197.6
P061433801105-20230910-01-01	2023-09-10	60197.6201	2023-09-10	60197.7523	60197.7
P061433801106-20230910-01-01	2023-09-10	60197.7523	2023-09-10	60197.8845	60197.8
P061433801107-20230910-01-01*	2023-09-10	60197.8845	2023-09-11	60198.0667	60198.0

Column 1 represents the Exposure IDs, taken for this complete analysis.

Column 2 and 4 represent the time (UT) of start and end of those exposures.

Column 3 and 5 represent the start and end MJDs of those exposures respectively.

Column 6 represents the average MJD for those exposure IDs.

Table 3. Properties estimated using timing analysis

Time (MJD)	QPO Frequency (Hz)			Q-Value			RMS			Shock Location ( $X_s$ )		
	LE	ME	HE	LE	ME	HE	LE	ME	HE	LE	ME	HE
(1)	(2)	(3)	(4)	(5)	(6)	(7)	(8)	(9)	(10)	(11)	(12)	(13)
2.19	0.20 ± 0.005	0.21 ± 0.003	0.20 ± 0.004	2.2 ± 0.5	3.6 ± 0.6	2.5 ± 0.6	18.0 ± 2.8	17.8 ± 2.2	23.3 ± 3.3	528.1 ± 72.5	523.5 ± 71.9	527.8 ± 72.5
2.39	0.23 ± 0.008	0.24 ± 0.002	0.24 ± 0.002	2.6 ± 0.7	4.4 ± 0.7	5.0 ± 0.7	17.5 ± 3.1	16.3 ± 1.8	19.7 ± 2.0	490.4 ± 67.3	475.3 ± 65.3	474.9 ± 65.2
2.60	0.30 ± 0.004	0.29 ± 0.004	0.30 ± 0.003	4.2 ± 0.7	3.2 ± 0.5	4.3 ± 0.6	16.3 ± 2.1	18.2 ± 2.0	21.7 ± 2.3	408.5 ± 56.1	416.1 ± 57.1	409.5 ± 56.2
2.80	0.34 ± 0.002	0.34 ± 0.003	0.34 ± 0.002	8.4 ± 1.6	5.5 ± 0.8	6.8 ± 1.4	14.2 ± 2.0	17.4 ± 1.8	20.3 ± 2.8	375.7 ± 51.6	377.8 ± 51.9	376.6 ± 51.7
2.89	0.37 ± 0.005	0.37 ± 0.003	0.38 ± 0.003	4.7 ± 1.0	5.2 ± 0.9	4.8 ± 0.7	16.1 ± 2.6	17.9 ± 2.4	21.9 ± 2.5	356.8 ± 49.0	356.7 ± 49.0	354.0 ± 48.6
3.10	0.43 ± 0.006	0.43 ± 0.005	0.44 ± 0.005	4.8 ± 1.0	4.6 ± 0.7	6.5 ± 0.7	16.8 ± 2.4	18.1 ± 2.1	19.7 ± 1.4	324.9 ± 44.6	324.2 ± 44.5	319.7 ± 43.9
3.30	0.44 ± 0.005	0.45 ± 0.002	0.45 ± 0.002	5.1 ± 1.0	7.0 ± 0.4	6.8 ± 0.4	16.9 ± 2.4	18.7 ± 1.2	22.2 ± 1.4	318.6 ± 43.7	315.7 ± 43.3	316.3 ± 43.4
3.39	0.50 ± 0.009	0.49 ± 0.005	0.47 ± 0.004	4.0 ± 0.7	4.4 ± 0.6	6.3 ± 1.2	17.8 ± 2.3	19.5 ± 2.0	21.8 ± 3.0	294.1 ± 40.4	295.8 ± 40.6	306.9 ± 42.1
3.50	0.50 ± 0.005	0.51 ± 0.005	0.51 ± 0.005	5.8 ± 1.1	6.0 ± 1.0	5.3 ± 0.9	16.9 ± 2.2	18.4 ± 2.1	23.0 ± 3.2	291.9 ± 40.1	289.5 ± 39.7	290.6 ± 39.9
3.69	0.52 ± 0.006	0.52 ± 0.004	0.52 ± 0.004	6.1 ± 0.9	5.6 ± 0.7	5.7 ± 0.6	16.5 ± 1.9	18.9 ± 1.6	22.7 ± 1.8	287.6 ± 39.5	286.4 ± 39.3	285.7 ± 39.2
3.80	0.56 ± 0.005	0.57 ± 0.004	0.57 ± 0.004	4.7 ± 0.7	6.7 ± 0.9	6.2 ± 0.8	17.2 ± 2.1	18.7 ± 1.8	22.6 ± 2.2	271.0 ± 37.2	270.0 ± 37.1	269.8 ± 37.0
4.10	0.63 ± 0.01	0.62 ± 0.006	0.61 ± 0.021	6.4 ± 2.7	8.7 ± 2.4	3.0 ± 0.9	15.5 ± 5.0	17.5 ± 3.8	19.3 ± 4.0	252.5 ± 34.7	254.0 ± 34.9	258.5 ± 35.5
4.19	0.67 ± 0.004	0.68 ± 0.003	0.68 ± 0.004	7.1 ± 1.0	6.5 ± 0.8	7.4 ± 1.1	16.2 ± 1.6	19.3 ± 1.7	22.3 ± 2.4	240.5 ± 33.0	240.0 ± 32.9	239.4 ± 32.9
4.30	0.71 ± 0.005	0.70 ± 0.003	0.70 ± 0.003	6.2 ± 0.8	7.2 ± 0.7	6.5 ± 0.6	16.8 ± 1.6	18.8 ± 1.4	22.7 ± 1.6	233.5 ± 32.0	234.1 ± 32.1	234.2 ± 32.1
4.50	0.69 ± 0.004	0.70 ± 0.004	0.69 ± 0.009	5.9 ± 0.2	4.1 ± 0.4	5.9 ± 0.5	18.0 ± 1.1	19.8 ± 1.5	21.9 ± 2.5	236.0 ± 32.4	234.4 ± 32.2	238.1 ± 32.7
4.60	0.71 ± 0.004	0.71 ± 0.004	0.72 ± 0.004	6.7 ± 1.0	7.2 ± 0.7	6.8 ± 0.8	16.6 ± 1.9	19.0 ± 1.6	22.3 ± 2.1	232.6 ± 31.9	232.2 ± 31.9	231.4 ± 31.8
5.39	0.89 ± 0.003	0.88 ± 0.003	0.90 ± 0.005	7.7 ± 0.2	6.3 ± 0.5	5.3 ± 0.5	17.0 ± 0.8	19.7 ± 1.2	22.9 ± 1.8	200.7 ± 27.5	201.0 ± 27.6	198.4 ± 27.2
5.50	0.87 ± 0.004	0.87 ± 0.004	0.86 ± 0.004	7.1 ± 0.8	7.2 ± 0.7	6.8 ± 0.8	16.0 ± 1.5	18.6 ± 1.5	21.7 ± 2.0	203.5 ± 27.9	203.7 ± 28.0	204.5 ± 28.1
5.69	0.81 ± 0.004	0.81 ± 0.003	0.81 ± 0.003	6.4 ± 0.9	7.4 ± 0.8	7.1 ± 0.8	15.6 ± 1.7	18.5 ± 1.6	21.6 ± 1.9	213.7 ± 29.3	213.8 ± 29.3	213.3 ± 29.3
5.89	0.98 ± 0.01	1.00 ± 0.011	1.00 ± 0.011	7.0 ± 1.3	6.0 ± 1.1	6.3 ± 1.4	14.9 ± 2.1	18.4 ± 2.7	21.3 ± 3.4	188.0 ± 25.8	185.8 ± 25.5	185.0 ± 25.4
6.10	1.11 ± 0.01	1.09 ± 0.011	1.01 ± 0.022	6.9 ± 1.4	6.8 ± 1.0	9.7 ± 4.4	15.8 ± 16.	18.1 ± 2.3	19.9 ± 6.8	172.9 ± 23.7	175.0 ± 24.0	183.8 ± 25.2
6.19	1.06 ± 0.005	1.06 ± 0.004	1.07 ± 0.004	7.4 ± 0.8	7.7 ± 0.6	6.5 ± 0.5	16.2 ± 1.3	19.1 ± 1.2	22.3 ± 1.5	178.8 ± 24.5	178.1 ± 24.4	177.2 ± 24.3
6.30	1.11 ± 0.005	1.13 ± 0.004	1.12 ± 0.004	8.6 ± 1.4	6.4 ± 0.5	6.5 ± 0.5	15.1 ± 1.7	19.3 ± 1.2	21.9 ± 1.4	172.5 ± 23.7	171.2 ± 23.5	171.7 ± 23.6
6.50	1.12 ± 0.006	1.12 ± 0.004	1.10 ± 0.009	6.3 ± 0.6	7.0 ± 0.5	5.5 ± 0.9	15.6 ± 1.3	19.2 ± 1.2	22.2 ± 2.9	171.5 ± 23.5	172.3 ± 23.6	173.8 ± 23.8
6.60	1.13 ± 0.005	1.13 ± 0.005	1.13 ± 0.005	5.8 ± 0.5	7.2 ± 0.7	6.3 ± 0.5	16.3 ± 1.2	18.7 ± 1.4	21.4 ± 1.5	171.0 ± 23.5	170.7 ± 23.4	170.5 ± 23.4
6.80	1.29 ± 0.009	1.30 ± 0.005	1.30 ± 0.007	8.7 ± 1.5	9.8 ± 1.2	8.9 ± 1.2	15.2 ± 2.3	18.7 ± 1.9	21.0 ± 2.3	156.5 ± 21.5	155.9 ± 21.4	156.0 ± 21.4
7.10	1.08 ± 0.007	1.09 ± 0.006	1.08 ± 0.009	6.6 ± 0.9	6.5 ± 0.8	6.5 ± 0.9	16.1 ± 1.6	18.7 ± 1.8	20.7 ± 2.3	176.5 ± 24.2	175.4 ± 24.1	176.0 ± 24.1
7.19	1.16 ± 0.004	1.15 ± 0.003	1.15 ± 0.003	6.4 ± 0.5	7.0 ± 0.4	6.8 ± 0.4	15.9 ± 1.0	19.1 ± 1.0	21.8 ± 1.2	168.1 ± 23.1	168.7 ± 23.1	168.8 ± 23.2
7.39	1.14 ± 0.006	1.14 ± 0.004	1.11 ± 0.009	6.9 ± 0.7	6.1 ± 0.5	6.6 ± 0.9	15.3 ± 1.2	19.2 ± 1.2	20.8 ± 2.3	169.8 ± 23.3	170.4 ± 23.4	173.5 ± 23.8
7.50	1.19 ± 0.007	1.21 ± 0.009	1.18 ± 0.009	5.1 ± 0.4	5.1 ± 0.5	4.6 ± 0.4	16.1 ± 1.1	19.6 ± 1.4	22.6 ± 1.5	165.1 ± 22.6	163.6 ± 22.4	166.5 ± 22.8
7.60	1.09 ± 0.007	1.10 ± 0.007	1.10 ± 0.006	4.4 ± 0.3	4.8 ± 0.4	4.5 ± 0.3	15.8 ± 1.1	19.4 ± 1.3	22.1 ± 1.4	174.8 ± 24.0	174.4 ± 23.9	174.4 ± 23.9
7.80	1.16 ± 0.007	1.16 ± 0.006	1.16 ± 0.006	6.5 ± 0.7	6.1 ± 0.5	5.0 ± 0.5	15.4 ± 1.4	18.6 ± 1.3	21.4 ± 2.0	167.7 ± 23.0	168.1 ± 23.1	167.9 ± 23.0
8.00	1.32 ± 0.01	1.32 ± 0.011	1.22 ± 0.009	6.0 ± 0.9	5.7 ± 0.7	13. ± 1.9	15.5 ± 2.0	18.7 ± 1.9	19.5 ± 3.0	153.8 ± 21.1	154.1 ± 21.1	162.3 ± 22.3
8.19	1.34 ± 0.005	1.33 ± 0.004	1.33 ± 0.005	7.2 ± 0.7	7.2 ± 0.5	6.2 ± 0.4	15.2 ± 1.2	18.7 ± 1.0	21.2 ± 1.2	152.7 ± 20.9	153.7 ± 21.1	153.6 ± 21.1
8.30	1.19 ± 0.008	1.19 ± 0.004	1.16 ± 0.005	5.1 ± 0.5	6.1 ± 0.4	6.6 ± 0.6	15.6 ± 1.2	19.0 ± 1.0	21.1 ± 1.7	164.9 ± 22.6	165.1 ± 22.6	168.0 ± 23.0
8.39	1.20 ± 0.006	1.20 ± 0.005	1.17 ± 0.005	6.5 ± 0.6	6.1 ± 0.5	8.5 ± 1.2	15.4 ± 1.2	18.8 ± 1.2	19.3 ± 2.2	164.0 ± 22.5	164.2 ± 22.5	166.8 ± 22.9
8.60	1.18 ± 0.007	1.20 ± 0.004	1.20 ± 0.005	7.6 ± 1.1	7.6 ± 0.7	6.9 ± 0.7	13.6 ± 1.5	18.5 ± 1.3	21.4 ± 1.7	166.3 ± 22.8	164.3 ± 22.5	164.5 ± 22.6
8.69	1.24 ± 0.006	1.24 ± 0.006	1.24 ± 0.005	6.3 ± 0.6	6.0 ± 0.5	5.6 ± 0.4	15.6 ± 1.1	19.1 ± 1.3	21.6 ± 1.4	160.9 ± 22.1	160.8 ± 22.1	160.6 ± 22.0
8.80	1.23 ± 0.009	1.23 ± 0.008	1.23 ± 0.008	8.7 ± 1.5	7.5 ± 1.0	7.3 ± 0.9	15.1 ± 2.1	18.4 ± 2.0	20.9 ± 2.2	161.7 ± 22.2	161.4 ± 22.1	161.6 ± 22.2

Continued on next page

Table 3 – continued from previous page

Time (MJD)	QPO Frequency (Hz)			Q-Value			RMS			Shock Location ( $X_s$ )		
	LE	ME	HE	LE	ME	HE	LE	ME	HE	LE	ME	HE
(1)	(2)	(3)	(4)	(5)	(6)	(7)	(8)	(9)	(10)	(11)	(12)	(13)
9.00	1.24 ± 0.008	1.23 ± 0.006	1.22 ± 0.009	7.3 ± 1.3	7.6 ± 0.3	10. ± 1.2	14.5 ± 2.0	19.6 ± 1.3	19.8 ± 1.3	160.8 ± 22.1	161.4 ± 22.1	162.2 ± 22.2
9.10	1.31 ± 0.005	1.30 ± 0.005	1.31 ± 0.005	6.8 ± 0.6	7.0 ± 0.5	6.6 ± 0.4	15.1 ± 1.1	18.5 ± 1.0	20.9 ± 1.1	155.1 ± 21.3	155.6 ± 21.3	155.1 ± 21.3
9.30	1.34 ± 0.006	1.34 ± 0.005	1.32 ± 0.007	6.2 ± 0.5	7.1 ± 0.7	7.3 ± 0.7	15.5 ± 1.1	18.6 ± 1.2	20.7 ± 1.6	152.8 ± 21.0	152.7 ± 20.9	153.8 ± 21.1
9.39	1.23 ± 0.008	1.25 ± 0.007	1.29 ± 0.007	4.5 ± 0.4	4.9 ± 0.3	6.5 ± 0.8	16.0 ± 1.3	19.6 ± 1.1	20.7 ± 2.1	161.2 ± 22.1	160.1 ± 22.0	156.6 ± 21.5
9.60	1.17 ± 0.005	1.17 ± 0.004	1.17 ± 0.004	7.6 ± 0.8	7.9 ± 0.8	6.5 ± 0.6	14.4 ± 1.2	17.7 ± 1.4	20.2 ± 1.5	167.1 ± 22.9	167.2 ± 22.9	167.0 ± 22.9
9.69	1.23 ± 0.01	1.23 ± 0.009	1.23 ± 0.009	4.0 ± 0.3	4.2 ± 0.3	4.1 ± 0.3	15.8 ± 1.0	18.6 ± 1.1	21.3 ± 1.2	161.3 ± 22.1	161.5 ± 22.2	161.6 ± 22.2
9.80	1.36 ± 0.01	1.33 ± 0.007	1.33 ± 0.009	5.5 ± 1.5	8.4 ± 0.4	5.9 ± 0.6	13.9 ± 2.7	18.5 ± 2.0	20.7 ± 1.9	151.4 ± 20.8	153.2 ± 21.0	153.2 ± 21.0
0.00	1.31 ± 0.01	1.32 ± 0.011	1.32 ± 0.011	7.0 ± 0.7	5.8 ± 1.2	11. ± 4.0	15.3 ± 2.1	18.5 ± 2.9	17.5 ± 4.4	154.7 ± 21.2	154.5 ± 21.2	154.0 ± 21.1
0.10	1.44 ± 0.01	1.44 ± 0.008	1.49 ± 0.008	5.3 ± 0.6	6.1 ± 0.5	7.1 ± 0.8	15.4 ± 1.3	18.6 ± 1.2	19.9 ± 1.6	145.6 ± 20.0	145.4 ± 19.9	142.1 ± 19.5
0.19	1.31 ± 0.005	1.32 ± 0.004	1.31 ± 0.003	6.6 ± 0.5	6.4 ± 0.4	6.3 ± 0.4	15.4 ± 1.0	18.6 ± 1.1	20.7 ± 1.1	154.9 ± 21.2	154.5 ± 21.2	154.6 ± 21.2
0.50	1.27 ± 0.006	1.27 ± 0.005	1.28 ± 0.005	7.2 ± 0.9	7.2 ± 0.7	8.4 ± 0.3	14.6 ± 1.5	18.1 ± 1.5	21.1 ± 1.0	158.5 ± 21.7	157.9 ± 21.7	157.6 ± 21.6
0.60	1.28 ± 0.007	1.30 ± 0.006	1.30 ± 0.006	7.3 ± 1.1	6.6 ± 0.5	6.0 ± 0.5	13.5 ± 1.4	18.1 ± 1.2	20.4 ± 1.4	157.1 ± 21.6	156.0 ± 21.4	155.9 ± 21.4
0.69	1.30 ± 0.007	1.30 ± 0.005	1.30 ± 0.005	6.6 ± 0.7	7.8 ± 0.8	7.0 ± 0.7	14.9 ± 1.3	17.8 ± 1.5	20.2 ± 1.7	156.1 ± 21.4	155.8 ± 21.4	155.7 ± 21.4
1.00	1.24 ± 0.008	1.23 ± 0.007	1.25 ± 0.011	6.5 ± 0.4	6.6 ± 0.7	7.1 ± 1.7	15.4 ± 1.2	18.5 ± 1.7	21.2 ± 3.9	161.1 ± 22.1	161.6 ± 22.2	159.5 ± 21.9
1.10	1.25 ± 0.007	1.25 ± 0.005	1.25 ± 0.005	5.0 ± 0.4	5.6 ± 0.3	5.4 ± 0.3	15.3 ± 1.0	18.6 ± 1.0	21.0 ± 1.1	159.8 ± 21.9	159.7 ± 21.9	159.7 ± 21.9
1.30	1.18 ± 0.009	1.17 ± 0.005	1.20 ± 0.004	6.0 ± 0.9	6.7 ± 0.5	7.5 ± 0.7	14.1 ± 1.5	17.6 ± 1.1	18.2 ± 1.4	166.0 ± 22.8	166.9 ± 22.9	163.9 ± 22.5
1.39	1.12 ± 0.008	1.13 ± 0.007	1.14 ± 0.009	4.7 ± 0.5	6.0 ± 0.5	4.9 ± 0.5	15.3 ± 1.2	18.0 ± 1.3	20.4 ± 1.9	171.9 ± 23.6	171.3 ± 23.5	170.0 ± 23.3
1.50	1.18 ± 0.006	1.17 ± 0.004	1.17 ± 0.004	5.8 ± 0.7	6.4 ± 0.6	6.6 ± 0.5	14.8 ± 1.4	17.5 ± 1.4	19.8 ± 1.4	166.5 ± 22.8	166.7 ± 22.9	167.1 ± 22.9
1.69	1.09 ± 0.007	1.08 ± 0.005	1.08 ± 0.005	4.6 ± 0.5	6.0 ± 0.5	6.0 ± 0.5	15.5 ± 1.4	17.9 ± 1.3	20.3 ± 1.4	175.5 ± 24.1	176.0 ± 24.1	175.8 ± 24.1
1.80	1.07 ± 0.01	1.08 ± 0.011	1.08 ± 0.009	5.9 ± 1.0	5.8 ± 1.0	5.4 ± 0.7	14.9 ± 2.0	17.1 ± 2.3	20.8 ± 2.5	177.5 ± 24.3	176.0 ± 24.1	175.9 ± 24.1
2.10	1.11 ± 0.008	1.12 ± 0.004	1.10 ± 0.005	6.0 ± 0.9	6.1 ± 0.4	6.5 ± 0.6	14.5 ± 1.6	17.7 ± 1.1	19.9 ± 1.4	172.7 ± 23.7	172.3 ± 23.6	174.2 ± 23.9
2.19	1.11 ± 0.007	1.10 ± 0.004	1.10 ± 0.004	5.9 ± 0.6	6.1 ± 0.5	6.0 ± 0.5	14.7 ± 1.2	17.6 ± 1.2	19.9 ± 1.2	173.4 ± 23.8	173.9 ± 23.9	173.7 ± 23.8
2.30	1.24 ± 0.01	1.25 ± 0.009	1.31 ± 0.011	4.1 ± 0.4	4.7 ± 0.3	7.0 ± 1.3	15.6 ± 1.2	17.8 ± 1.0	18.6 ± 2.9	161.0 ± 22.1	159.7 ± 21.9	155.1 ± 21.3
2.50	1.50 ± 0.01	1.49 ± 0.009	1.48 ± 0.009	4.5 ± 0.4	5.4 ± 0.4	5.5 ± 0.2	14.1 ± 1.0	17.7 ± 1.0	20.9 ± 0.8	141.9 ± 19.5	142.1 ± 19.5	143.0 ± 19.6
2.60	1.45 ± 0.009	1.46 ± 0.006	1.46 ± 0.006	5.5 ± 0.7	6.2 ± 0.5	6.0 ± 0.4	14.7 ± 1.4	18.0 ± 1.1	20.1 ± 1.2	144.8 ± 19.9	143.9 ± 19.7	143.9 ± 19.7
2.69	1.37 ± 0.007	1.38 ± 0.006	1.37 ± 0.007	8.0 ± 1.1	8.0 ± 0.8	7.2 ± 0.8	14.3 ± 1.4	17.3 ± 1.5	19.5 ± 1.6	150.4 ± 20.6	149.8 ± 20.5	150.1 ± 20.6
3.00	1.45 ± 0.01	1.46 ± 0.005	1.46 ± 0.009	7.7 ± 1.2	8.1 ± 0.8	8.0 ± 1.3	13.3 ± 1.5	17.2 ± 1.3	18.4 ± 2.4	145.0 ± 19.9	144.4 ± 19.8	144.1 ± 19.8
3.10	1.47 ± 0.009	1.47 ± 0.005	1.47 ± 0.004	6.4 ± 0.6	6.8 ± 0.4	6.6 ± 0.4	14.0 ± 1.0	17.5 ± 0.9	19.3 ± 1.0	143.6 ± 19.7	143.3 ± 19.6	143.5 ± 19.7
3.30	1.41 ± 0.008	1.40 ± 0.004	1.42 ± 0.006	5.3 ± 0.5	7.4 ± 0.5	7.6 ± 0.8	14.5 ± 1.2	17.4 ± 1.0	19.1 ± 1.6	147.3 ± 20.2	147.9 ± 20.3	146.7 ± 20.1
3.39	1.37 ± 0.01	1.35 ± 0.006	1.39 ± 0.008	5.5 ± 0.7	5.7 ± 0.4	5.6 ± 0.5	14.3 ± 1.3	17.7 ± 1.0	19.5 ± 1.3	150.6 ± 20.7	152.1 ± 20.9	149.3 ± 20.5
4.10	1.30 ± 0.01	1.28 ± 0.008	1.28 ± 0.009	3.5 ± 0.3	4.3 ± 0.2	3.7 ± 0.2	15.3 ± 1.1	17.4 ± 0.8	20.5 ± 0.9	155.6 ± 21.3	157.0 ± 21.5	157.1 ± 21.6
4.19	1.28 ± 0.01	1.28 ± 0.006	1.25 ± 0.006	5.7 ± 0.6	5.8 ± 0.5	7.2 ± 0.8	14.7 ± 1.3	17.5 ± 1.1	19.1 ± 1.6	157.4 ± 21.6	157.5 ± 21.6	160.1 ± 22.0
4.39	1.39 ± 0.01	1.39 ± 0.005	1.39 ± 0.006	5.3 ± 0.8	6.5 ± 0.5	6.3 ± 0.6	14.4 ± 1.4	17.4 ± 1.0	19.0 ± 1.3	148.6 ± 20.4	149.2 ± 20.5	148.7 ± 20.4
4.50	1.49 ± 0.01	1.49 ± 0.007	1.49 ± 0.007	5.0 ± 0.5	5.9 ± 0.4	5.6 ± 0.3	14.7 ± 1.1	17.6 ± 1.0	19.8 ± 1.1	142.0 ± 19.5	142.3 ± 19.5	142.5 ± 19.5
4.89	1.39 ± 0.01	1.40 ± 0.011	1.47 ± 0.033	8.7 ± 4.1	7.5 ± 1.5	7.5 ± 5.2	12.0 ± 4.3	16.3 ± 2.5	15.4 ± 6.8	149.0 ± 20.4	148.3 ± 20.3	143.6 ± 19.7
5.00	1.30 ± 0.006	1.30 ± 0.005	1.30 ± 0.005	6.1 ± 0.2	5.8 ± 0.4	5.4 ± 0.4	15.3 ± 0.7	17.0 ± 1.0	19.2 ± 1.2	155.8 ± 21.4	155.9 ± 21.4	155.9 ± 21.4
5.19	1.30 ± 0.01	1.31 ± 0.006	1.29 ± 0.006	5.0 ± 0.7	5.6 ± 0.4	5.6 ± 0.5	14.3 ± 1.3	17.3 ± 1.0	18.8 ± 1.3	155.4 ± 21.3	154.7 ± 21.2	156.3 ± 21.4
5.30	1.39 ± 0.009	1.38 ± 0.005	1.38 ± 0.007	5.9 ± 0.7	7.2 ± 0.6	6.8 ± 0.8	14.0 ± 1.3	16.5 ± 1.1	18.3 ± 1.7	149.2 ± 20.5	149.5 ± 20.5	149.9 ± 20.6
5.39	1.39 ± 0.01	1.39 ± 0.005	1.39 ± 0.004	6.0 ± 0.8	6.6 ± 0.5	5.8 ± 0.4	13.6 ± 1.3	16.7 ± 1.0	21.5 ± 1.0	149.2 ± 20.5	148.7 ± 20.4	148.7 ± 20.4
5.60	1.29 ± 0.009	1.31 ± 0.006	1.32 ± 0.006	6.9 ± 0.9	6.2 ± 0.5	5.6 ± 0.4	13.5 ± 1.3	17.0 ± 1.1	19.5 ± 1.1	156.4 ± 21.5	155.2 ± 21.3	154.5 ± 21.2
5.69	1.37 ± 0.01	1.37 ± 0.008	1.35 ± 0.008	6.2 ± 1.6	7.6 ± 1.0	6.1 ± 0.8	13.4 ± 2.6	15.8 ± 1.7	17.6 ± 1.9	150.7 ± 20.7	150.6 ± 20.6	151.6 ± 20.8
6.00	1.39 ± 0.01	1.40 ± 0.006	1.39 ± 0.006	5.3 ± 0.8	5.9 ± 0.4	5.6 ± 0.4	13.8 ± 1.5	16.9 ± 0.9	18.8 ± 1.0	148.8 ± 20.4	148.2 ± 20.3	148.9 ± 20.4

Continued on next page

Table 3 – continued from previous page

Time	QPO Frequency (Hz)			Q-Value			RMS			Shock Location ( $X_s$ )		
(MJD)	LE	ME	HE	LE	ME	HE	LE	ME	HE	LE	ME	HE
(1)	(2)	(3)	(4)	(5)	(6)	(7)	(8)	(9)	(10)	(11)	(12)	(13)
6.19	$1.37 \pm 0.008$	$1.38 \pm 0.004$	$1.39 \pm 0.006$	$7.5 \pm 1.2$	$7.3 \pm 0.6$	$7.5 \pm 0.8$	$13.2 \pm 1.5$	$16.4 \pm 1.1$	$17.9 \pm 1.5$	$150.5 \pm 20.6$	$149.6 \pm 20.5$	$149.3 \pm 20.5$
6.30	$1.24 \pm 0.01$	$1.26 \pm 0.006$	$1.25 \pm 0.009$	$6.1 \pm 0.9$	$6.8 \pm 0.7$	$6.6 \pm 1.0$	$13.8 \pm 1.5$	$16.2 \pm 1.2$	$18.3 \pm 2.0$	$160.6 \pm 22.0$	$158.6 \pm 21.8$	$160.0 \pm 21.9$
6.39	$1.23 \pm 0.01$	$1.24 \pm 0.007$	$1.24 \pm 0.006$	$5.0 \pm 0.8$	$5.2 \pm 0.4$	$4.8 \pm 0.3$	$14.0 \pm 1.5$	$17.0 \pm 1.0$	$19.4 \pm 1.2$	$161.7 \pm 22.2$	$160.4 \pm 22.0$	$161.0 \pm 22.1$
6.60	$1.11 \pm 0.008$	$1.12 \pm 0.005$	$1.12 \pm 0.004$	$7.6 \pm 1.3$	$6.7 \pm 0.6$	$5.7 \pm 0.5$	$13.8 \pm 1.9$	$20.4 \pm 1.2$	$18.8 \pm 1.3$	$172.6 \pm 23.7$	$171.9 \pm 23.6$	$172.1 \pm 23.6$
7.00	$1.29 \pm 0.008$	$1.25 \pm 0.006$	$1.30 \pm 0.005$	$5.6 \pm 0.2$	$8.2 \pm 0.2$	$5.6 \pm 0.4$	$15.2 \pm 0.8$	$17.4 \pm 3.7$	$18.7 \pm 1.1$	$156.3 \pm 21.4$	$159.4 \pm 21.9$	$155.4 \pm 21.3$
7.10	$1.45 \pm 0.008$	$1.45 \pm 0.005$	$1.45 \pm 0.005$	$7.0 \pm 0.9$	$7.9 \pm 0.7$	$9.3 \pm 0.5$	$13.1 \pm 1.3$	$15.8 \pm 1.2$	$18.4 \pm 1.8$	$144.9 \pm 19.9$	$144.7 \pm 19.8$	$144.8 \pm 19.9$
7.30	$1.50 \pm 0.008$	$1.51 \pm 0.005$	$1.51 \pm 0.007$	$5.8 \pm 0.7$	$7.3 \pm 0.5$	$7.0 \pm 0.6$	$13.3 \pm 1.3$	$16.7 \pm 1.0$	$18.3 \pm 1.4$	$141.7 \pm 19.4$	$141.2 \pm 19.4$	$140.9 \pm 19.3$
7.39	$1.42 \pm 0.009$	$1.43 \pm 0.004$	$1.42 \pm 0.005$	$6.9 \pm 1.1$	$6.6 \pm 0.4$	$5.8 \pm 0.4$	$13.2 \pm 1.4$	$16.4 \pm 1.0$	$18.4 \pm 1.0$	$146.8 \pm 20.1$	$146.5 \pm 20.1$	$146.8 \pm 20.1$
7.60	$1.45 \pm 0.009$	$1.43 \pm 0.005$	$1.43 \pm 0.005$	$6.4 \pm 1.1$	$6.8 \pm 0.5$	$6.7 \pm 0.5$	$12.9 \pm 1.6$	$16.0 \pm 1.0$	$17.3 \pm 1.1$	$144.6 \pm 19.8$	$146.3 \pm 20.1$	$145.9 \pm 20.0$
7.80	$1.69 \pm 0.02$	$1.79 \pm 0.011$	$1.78 \pm 0.011$	$5.6 \pm 1.8$	$4.0 \pm 0.4$	$8.3 \pm 2.4$	$13.1 \pm 3.2$	$17.3 \pm 1.5$	$15.0 \pm 3.1$	$130.7 \pm 17.9$	$125.7 \pm 17.2$	$126.3 \pm 17.3$
8.00	$1.85 \pm 0.01$	$1.84 \pm 0.004$	$1.84 \pm 0.005$	$6.9 \pm 0.8$	$6.9 \pm 0.3$	$6.6 \pm 0.3$	$12.5 \pm 1.2$	$16.6 \pm 0.7$	$18.3 \pm 0.8$	$123.0 \pm 16.9$	$123.7 \pm 17.0$	$123.4 \pm 16.9$

In column 1, we have listed the MJD-60180 (to save space) of the exposure IDs we used.  
Columns 2, 3, & 4 represent the QPO frequency in LE, ME, and HE energy bands respectively.  
Columns 5, 6, & 7 represent the Q-values of QPOs in LE, ME, and HE energy bands respectively.  
Columns 8, 9, & 10 represent the QPO RMS (%) in LE, ME, and HE energy bands respectively.  
Columns 11, 12, & 13 represent the shock location in LE, ME, and HE energy bands respectively.

Table 4. Properties from spectral analysis

Time	TBabs	gabs			diskbb		power-law		Gaussian			pexrav					
MJD (Day)	$N_H$ ( $\text{cm}^{-2}$ )	$E_{\text{abs}}$ (keV)	$\sigma_{\text{abs}}$ (keV)	$N_{\text{abs}}$ (keV)	$T_{\text{in}}$ (keV)	Norm	$\Gamma$	Norm	$E_g$ (keV)	$\sigma_g$ (keV)	Norm ( $\text{ph}/\text{cm}^2/\text{s}$ )	$\Gamma$	$E_{\text{cut}}$ (keV)	$R_{\text{ref}}$	$\cos(i)$	Norm	$\chi^2/DOF$
(1)	(2)	(3)	(4)	(5)	(6)	(7)	(8)	(9)	(10)	(11)	(12)	(13)	(14)	(15)	(16)	(17)	(18)
60181.4	0.1859 ± 3.1E-3	1.780 ± 3.2E-2	0.4000 ± 2.2E-2	0.1797 ± 7.5E-3	0.1797 ± 2.2E-3	1.8E+05 ± 1.6E+3	2.1238 ± 9.4E-3	13.084 ± 0.969	5.252 ± 5.4E-2	1.920 ± 6.9E-2	0.8232 ± 3.5E-2	1.1406 ± 7.1E-2	26.25 ± 0.98	0.4000 ± 4.5E-3	0.4912 ± 6.2E-3	3.32 ± 0.37	1384.50/1401
60181.6	0.1859 ± 6.8E-3	1.798 ± 6.1E-2	0.2289 ± 3.6E-2	1.1E-2 ± 1.4E-3	0.1999 ± 1.1E-2	1.9E+05 ± 1.1E+3	2.1612 ± 1.9E-2	18.201 ± 1.925	5.482 ± 5.1E-2	1.621 ± 6.1E-2	0.6342 ± 2.9E-2	0.9422 ± 8.4E-2	20.33 ± 1.15	0.5000 ± 5.0E-2	0.1944 ± 1.6E-2	2.70 ± 0.70	1375.43/1401
60181.7	0.1859 ± 5.3E-3	1.650 ± 4.8E-2	2.40E-2 ± 2.8E-2	1.0E-2 ± 1.1E-3	0.2989 ± 1.7E-2	1.1E+05 ± 2.6E+3	2.1053 ± 1.8E-2	15.134 ± 1.748	5.621 ± 4.5E-2	2.917 ± 5.6E-2	20.2047 ± 2.3E-2	1.0043 ± 6.1E-2	20.07 ± 0.86	0.4986 ± 8.2E-4	5.1E-2 ± 2.1E-2	4.45 ± 0.68	1341.34/1283
60182.1	0.1859 ± 9.0E-3	1.650 ± 3.0E-2	2.40E-2 ± 2.7E-2	1.0E-2 ± 6.9E-3	0.2650 ± 1.8E-4	1.1E+05 ± 3.8E+3	2.1553 ± 9.5E-2	18.462 ± 4.4E-2	5.552 ± 8.5E-2	0.877 ± 0.1067	0.2584 ± 5.6E-2	1.0053 ± 0.1639	17.84 ± 2.30	0.4740 ± 8.6E-2	6.1E-2 ± 1.0E-2	25.26 ± 1.8E-2	1235.38/1283
60182.9	0.3859 ± 1.4E-2	1.950 ± 0.1323	0.3656 ± 2.1E-3	3.1E-2 ± 1.9E-3	0.3949 ± 1.9E-4	1.1E+05 ± 3.8E+3	1.9556 ± 1.6E-2	36.0786 ± 3.9E-2	5.417 ± 5.1E-2	0.989 ± 6.8E-2	0.3876 ± 6.3E-2	1.3568 ± 0.2559	20.18 ± 3.47	0.4990 ± 8.1E-5	5.0E-2 ± 2.1E-3	17.2 ± 1.5E-2	1220.62/1283
60183.1	0.3859 ± 4.7E-2	1.901 ± 1.6E-2	0.4000 ± 2.3E-2	5.7E-2 ± 1.9E-3	0.3353 ± 3.5E-3	7.8E+06 ± 3.6E+4	1.9805 ± 2.5E-2	6.2591 ± 3.4086	5.288 ± 5.8E-2	1.255 ± 6.4E-2	20.6211 ± 5.9E-2	1.3521 ± 6.9E-2	20.64 ± 0.71	5.7E-2 ± 4.7E-3	5.0E-2 ± 5.3E-3	17.4 ± 1.1E-2	1004.79/1313
60183.8	0.3859 ± 8.3E-3	1.764 ± 6.5E-3	0.3621 ± 8.7E-3	0.1800 ± 2.6E-3	0.2855 ± 2.6E-4	2.3E+06 ± 1.9E+4	1.9641 ± 3.2E-2	35.1858 ± 4.6E-2	5.478 ± 9.9E-2	1.053 ± 8.4E-2	20.4529 ± 8.8E-2	1.4714 ± 8.9E-2	22.18 ± 1.71	1.0E-2 ± 6.7E-3	5.0E-2 ± 3.6E-3	32.9 ± 1.8E-2	1149.55/1313
60184.6	0.3500 ± 8.2E-3	1.768 ± 6.1E-3	0.3537 ± 8.3E-3	0.1799 ± 6.7E-3	0.2793 ± 2.5E-4	2.9E+06 ± 2.4E+4	1.9883 ± 1.9E-3	5.6874 ± 2.9E-2	5.446 ± 9.5E-2	1.056 ± 8.0E-2	20.5005 ± 9.5E-2	1.5152 ± 9.0E-2	22.08 ± 1.77	1.0E-2 ± 6.9E-3	5.0E-2 ± 3.7E-3	32.71 ± 1.9E-2	1201.52/1303
60185.4	0.3500 ± 7.5E-3	1.799 ± 5.8E-3	0.3689 ± 7.7E-3	0.1800 ± 5.7E-3	0.2984 ± 2.2E-4	2.0E+06 ± 1.3E+4	2.0041 ± 1.9E-3	36.3291 ± 2.9E-2	5.342 ± 8.8E-2	2.934 ± 8.3E-2	20.4323 ± 9.5E-2	1.5314 ± 9.8E-2	21.63 ± 1.87	1.0E-2 ± 6.4E-3	5.0E-2 ± 3.6E-3	38.2 ± 1.8E-2	1111.05/1285
60186.2	0.3500 ± 8.4E-3	1.756 ± 6.9E-3	0.3762 ± 6.9E-3	0.1800 ± 8.9E-3	0.3189 ± 2.8E-4	1.2E+06 ± 8.918.9	2.1058 ± 1.7E-3	39.6845 ± 3.6E-2	5.305 ± 3.6E-2	1.015 ± 0.1152	0.5269 ± 9.5E-2	1.5823 ± 0.1425	22.04 ± 2.65	1.0E-2 ± 6.9E-3	5.0E-2 ± 1.9E-3	39.0 ± 2.2E-2	1122.93/1285
60187.1	0.3276 ± 5.6E-3	1.950 ± 2.2E-2	0.4000 ± 2.9E-2	0.1306 ± 4.2E-3	0.3227 ± 3.6E-4	1.2E+06 ± 1.2E+4	2.0974 ± 2.5E-3	39.5144 ± 4.2E-2	5.354 ± 0.1790	0.948 ± 0.1523	0.4538 ± 6.6E-3	1.5803 ± 0.2594	21.77 ± 4.83	1.3E-2 ± 4.2E-3	3.5E-2 ± 9.1E-3	42.86 ± 2.4E-2	996.48/1285
60187.2	0.3500 ± 7.8E-3	1.799 ± 6.4E-3	0.3917 ± 8.6E-3	0.1800 ± 6.1E-3	0.3273 ± 2.5E-4	1.0E+06 ± 6.693.9	2.126 ± 1.5E-3	30.804 ± 3.5E-2	5.296 ± 0.1264	0.977 ± 0.1035	0.4905 ± 0.1346	1.6026 ± 0.1668	22.55 ± 3.18	1.0E-2 ± 6.6E-3	5.0E-2 ± 3.5E-4	42.8 ± 2.1E-2	1078.22/1285
60188.0	0.3166 ± 4.8E-3	1.815 ± 1.3E-2	0.4000 ± 3.3E-2	0.1113 ± 3.4E-3	0.3618 ± 4.1E-4	4.1E+05 ± 3.669.1	2.1735 ± 2.3E-3	35.329 ± 5.5E-2	5.309 ± 0.1971	1.904 ± 2.7E-2	20.3923 ± 9.6E-3	1.6310 ± 0.3514	20.97 ± 3.10	0.5000 ± 7.7E-2	8.8E-2 ± 9.6E-2	37.8 ± 3.0E-2	1057.80/1313
60189.0	0.1203 ± 7.1E-3	1.950 ± 3.4E-2	0.2443 ± 1.9E-2	3.9E-2 ± 2.1E-3	0.3598 ± 6.3E-4	2.4E+05 ± 3216.2	2.1753 ± 2.3E-3	13.528 ± 4.9E-2	5.437 ± 0.1067	1.000 ± 2.5E-2	20.4316 ± 4.2E-2	1.6133 ± 0.3538	22.06 ± 6.38	0.5000 ± 1.1E-2	5.2E-2 ± 5.8E-2	32.78 ± 2.7E-2	1016.91/1313
60189.1	0.1200 ± 7.6E-3	1.712 ± 1.1E-2	0.3999 ± 2.9E-2	0.1136 ± 3.5E-3	0.3412 ± 4.6E-4	3.8E+05 ± 4145.9	2.1434 ± 1.6E-3	10.399 ± 3.5E-2	5.513 ± 1.7E-2	1.000 ± 2.9E-2	20.4408 ± 5.3E-3	1.6954 ± 4.5E-2	24.35 ± 7E-2	1.0E-2 ± 6.6E-3	5.0E-2 ± 3.7E-2	33.21 ± 2.2E-2	1466.04/1431
60190.1	0.1200 ± 8.3E-3	1.950 ± 2.6E-2	0.2363 ± 1.4E-2	4.4E-2 ± 1.9E-3	0.3375 ± 5.6E-4	3.2E+05 ± 4960.2	2.1789 ± 1.9E-3	11.929 ± 4.3E-2	5.542 ± 2.4E-2	1.000 ± 4.0E-2	20.3701 ± 6.2E-3	1.7417 ± 5.5E-4	24.79 ± 0.10	0.1000 ± 2.4E-2	0.1000 ± 4.1E-2	33.2 ± 2.7E-2	1271.40/1431
60191.0	0.2632 ± 4.6E-3	1.950 ± 3.9E-2	0.2229 ± 2.2E-2	3.0E-2 ± 4.2E-3	0.3650 ± 4.9E-4	2.7E+05 ± 2821.2	2.0287 ± 3.1E-3	36.6459 ± 3.8E-2	5.473 ± 3.3E-2	2.899 ± 2.7E-2	20.2641 ± 6.6E-3	1.6578 ± 5.8E-4	23.46 ± 0.11	0.2205 ± 2.8E-2	9.8E-2 ± 1.8E-2	30.6 ± 2.6E-2	1124.73/1431
60191.1	0.3086 ± 0.0030	-	-	-	0.4137 ± 0.0017	9.8E+04 ± 1587.2	2.1029 ± 0.0085	8.423 ± 0.8943	5.509 ± 0.0500	1.000 ± 0.0645	0.3533 ± 0.030	1.6820 ± 0.0619	25.08 ± 0.87	1.0E-2 ± 0.004	5.0E-2 ± 0.0057	30.3 ± 0.328	1250.10/1434
60192.2	0.3376 ± 0.0067	-	-	-	0.4183 ± 0.0085	9.2E+04 ± 1091.2	2.0389 ± 0.0173	6.182 ± 1.7767	5.515 ± 0.0472	1.000 ± 0.0570	0.3479 ± 0.025	1.6420 ± 0.0732	25.44 ± 1.03	1.0E-2 ± 0.005	5.0E-2 ± 0.0048	27.7 ± 0.621	1232.74/1434
60193.4	0.2517 ± 0.0052	-	-	-	0.4298 ± 0.0131	6.4E+04 ± 2579.2	2.2491 ± 0.0164	16.79 ± 1.6134	5.471 ± 0.0416	1.000 ± 0.0523	0.4039 ± 0.020	1.6530 ± 0.0531	24.97 ± 0.77	1.1E-2 ± 0.000	0.1000 ± 0.0094	23.7 ± 0.603	1496.21/1434
60194.1	0.3500 ± 0.0055	-	-	-	0.4204 ± 0.0035	1.0E+05 ± 4960.0	2.0766 ± 0.0192	7.510 ± 1.8635	5.460 ± 0.0407	0.689 ± 0.0495	0.1901 ± 0.021	1.6560 ± 0.0540	25.60 ± 0.77	1.0E-2 ± 0.009	5.0E-2 ± 0.003	26.9 ± 0.0061	1177.08/1434
60194.5	0.1200 ± 0.0023	-	-	-	0.4526 ± 0.0001	2.5E+04 ± 2083.2	2.2001 ± 0.0944	10.89 ± 0.3239	5.572 ± 0.0951	1.000 ± 0.1342	0.4107 ± 0.066	1.8360 ± 0.1095	29.50 ± 1.89	0.52 ± 0.008	0.10 ± 0.005	32.0 ± 0.0241	1697.00/1428
60195.0	0.3500 ± 0.0089	-	-	-	0.4204 ± 0.0001	9.8E+04 ± 3273.6	2.0180 ± 0.0866	5.491 ± 0.0406	5.525 ± 0.0787	0.713 ± 0.0997	0.1504 ± 0.049	1.6800 ± 0.1429	26.42 ± 2.06	1.0E-2 ± 0.007	5.0E-2 ± 0.008	27.9 ± 0.0092	1048.98/1432
60195.2	0.3500 ± 0.0088	-	-	-	0.4240 ± 0.0002	9.1E+04 ± 6844.8	2.0143 ± 0.0024	5.500 ± 0.0609	5.504 ± 0.0407	0.728 ± 0.0504	0.1716 ± 0.035	1.6820 ± 0.1555	26.52 ± 1.88	1.0E-2 ± 0.072	5.0E-2 ± 0.0030	27.9 ± 0.007	1070.82/1432
60195.6	0.1202 ± 0.0468	-	-	-	0.3834 ± 0.0027	5.7E+04 ± 3571.2	2.1645 ± 0.0228	8.874 ± 1.1461	5.593 ± 0.0537	1.000 ± 0.0598	0.4149 ± 0.051	1.8000 ± 0.0601	30.54 ± 0.63	0.42 ± 0.004	9.9E-2 ± 0.0049	29.0 ± 0.009	1515.80/1430
60196.0	0.3500 ± 0.0082	-	-	-	0.4296 ± 0.0002	8.4E+04 ± 1884.8	2.0542 ± 0.0029	6.241 ± 0.0424	5.515 ± 0.0916	0.736 ± 0.0785	0.1505 ± 0.077	1.7180 ± 0.0776	27.78 ± 1.53	1.0E-2 ± 0.006	5.0E-2 ± 0.0033	28.6 ± 0.015	1048.18/1434
60196.2	0.3500 ± 0.0081	-	-	-	0.4315 ± 0.0001	8.4E+04 ± 2380.8	2.0562 ± 0.0017	6.572 ± 0.0267	5.548 ± 0.0879	0.657 ± 0.0748	0.1340 ± 0.083	1.6910 ± 0.0784	26.73 ± 1.58	6.4E-2 ± 0.006	5.0E-2 ± 0.0034	27.3 ± 0.016	1036.34/1434
60196.6	0.1201 ± 0.0074	-	-	-	0.3545 ± 0.0001	1.0E+05 ± 1289.6	2.0491 ± 0.0017	5.511 ± 0.0267	5.607 ± 0.0814	1.000 ± 0.0776	0.3877 ± 0.083	1.7610 ± 0.0854	29.76 ± 1.67	0.44 ± 0.005	9.9E-2 ± 0.0033	27.6 ± 0.015	1517.31/1434
60197.0	0.3453 ± 0.0083	-	-	-	0.4326 ± 0.0002	7.7E+04 ± 8846.9	1.9867 ± 0.0015	4.390 ± 0.0332	5.569 ± 0.0333	0.707 ± 0.1077	0.1417 ± 0.083	1.6960 ± 0.1242	28.60 ± 2.37	0.14 ± 0.006	5.0E-2 ± 0.0017	27.0 ± 0.019	1009.58/1434
60197.1	0.3500 ± 0.0055	-	-	-	0.4333 ± 0.0002	7.9E+04 ± 1190.4	2.0631 ± 0.0022	6.810 ± 0.0387	5.441 ± 0.1657	0.749 ± 0.1424	0.1654 ± 0.005	1.7280 ± 0.2261	27.24 ± 4.33	0.31 ± 0.003	5.0E-2 ± 0.0008	27.5 ± 0.021	1108.23/1434
60197.6	0.1200 ± 0.0077	-	-	-	0.4298 ± 0.0001	2.8E+04 ± 6640.3	2.2020 ± 0.0013	10.47 ± 0.0323	5.614 ± 0.1170	1.000 ± 0.0967	0.3532 ± 0.017	1.8330 ± 0.1454	31.74 ± 2.85	0.50 ± 0.006	0.10 ± 0.0003	28.2 ± 0.018	1455.99/1434
60198.0	0.3500 ± 0.0047	-	-	-	0.4176 ± 0.0003	9.1E+04 ± 3577.2	2.1415 ± 0.0020	8.122 ± 0.0507	5.519 ± 0.1825	0.548 ± 0.0252	0.1061 ± 0.008	1.8990 ± 0.3064	31.93 ± 2.78	0.50 ± 0.007	8.7E-2 ± 0.0089	35.7 ± 0.026	1087.43/1434

Column 1 represents the MJD of those respective Exposure IDs for which we have performed spectral analysis.

Column 2 gives the values of hydrogen column densities ( $N_H$ ) of those analyzed exposures.

Columns 3, 4, & 5 give the values of the parameters of the ‘gabs’ model.

Columns 6 & 7 give the model fitted values of the parameters from the ‘diskbb’ model.

Columns 8 & 9 give the model fitted values of the parameters from the ‘power-law’ model.

Columns 10, 11, & 12 give the model fitted values of the parameters from the ‘Gaussian’ model.

Columns 13–17 give the model fitted values of the parameters from the ‘pexrav’ model.

Column 18 gives  $\chi^2/DOF$  values of the respective spectral fits.

